THE DEEP PROPAGATING GRAVITY WAVE EXPERIMENT (DEEPWAVE)

An Airborne and Ground-Based Exploration of Gravity Wave Propagation and Effects from Their Sources throughout the Lower and Middle Atmosphere

BY DAVID C. FRITTS, RONALD B. SMITH, MICHAEL J. TAYLOR, JAMES D. DOYLE, STEPHEN D. ECKERMANN, ANDREAS DÖRNBRACK, MARKUS RAPP, BIFFORD P. WILLIAMS, P.-DOMINIQUE PAUTET, KATRINA BOSSERT, NEAL R. CRIDDLE, CAROLYN A. REYNOLDS, P. ALEX REINECKE, MICHAEL UDDSTROM, MICHAEL J. REVELL, RICHARD TURNER, BERND KAIFLER, JOHANNES S. WAGNER, TYLER MIXA, CHRISTOPHER G. KRUSE, ALISON D. NUGENT, CAMPBELL D. WATSON, SONJA GISINGER, STEVEN M. SMITH, RUTH S. LIEBERMAN, BRIAN LAUGHMAN, JAMES J. MOORE, WILLIAM O. BROWN, JULIE A. HAGGERTY, ALISON ROCKWELL, GREGORY J. STOSSMEISTER, STEVEN F. WILLIAMS, GONZALO HERNANDEZ, DAMIAN J. MURPHY, ANDREW R. KLEKOCIUK, IAIN M. REID, AND JUN MA

The DEEPWAVE experiment employed extensive airborne and ground-based measurements to provide new insights into gravity wave dynamics.

The Deep Propagating Gravity Wave Experiment (DEEPWAVE) was the first comprehensive measurement program devoted to quantifying the evolution of gravity waves (GWs) arising from sources at lower altitudes as they propagate, interact with mean and other wave motions, and ultimately dissipate from Earth's surface into the mesosphere and lower thermosphere (MLT). Research goals motivating the DEEPWAVE measurement program are summarized in Table 1. To achieve our research goals, DEEPWAVE needed to sample regions having large horizontal extents because of large horizontal GW propagation distances for some GW sources. DEEPWAVE accomplished this goal through airborne and ground-based (GB) measurements that together provided sensitivity to multiple GW sources and their propagation to, and effects at, higher altitudes. DEEPWAVE was performed over and around the GW "hotspot" region of New Zealand (Fig.1, top) during austral winter, when strong vortex edge westerlies provide a stable environment for deep GW propagation into the MLT.

DEEPWAVE airborne measurements employed two research aircraft during a core 6-week airborne field program based at Christchurch, New Zealand, from 6 June to 21 July 2014. The National Science

Table 1. Science goals.
• Detailed measurements and modeling of GW sources, propagation, momentum fluxes, instabilities, and effects, from their sources in the troposphere into the MLT, in the GW hotspot over New Zealand and Tasmania, and the Southern Ocean.
• Understanding GW variations throughout the stratosphere and the implications for momentum flux divergence and drag.
• Studies of GW propagation, filtering by mean and large-scale motions, and nonlinear interactions and instabilities impacting GW penetration into the MLT, where GW momentum deposition has major influences on circulation, structure, and variability.
• Predictability studies of GW sources, propagation, breaking, and their influences on forecasting.
• Characterization of GW sources, scales, amplitudes, intermittency, and momentum transport throughout the atmosphere as inputs to improved GW parameterizations for NWP, climate, and general circulation models.

Foundation (NSF)/National Center for Atmospheric Research (NCAR) Gulfstream V (GV) provided in situ, dropsonde, and microwave temperature profiler (MTP) measurements extending from Earth's surface to ~20 km throughout the core field program (see Table 2). The GV also carried three new instruments designed specifically to address DEEPWAVE science goals: 1) a Rayleigh lidar measuring densities and temperatures from ~20 to 60 km, 2) a sodium resonance lidar measuring sodium densities and temperatures from ~75 to 100 km, and 3) an advanced mesosphere temperature mapper (AMTM) measuring temperatures in a horizontal plane at ~87 km with a field of view (FOV) of ~120 km along track and 80 km cross track. AMTM measurements were augmented by two side-viewing infrared (IR) airglow "wing" cameras also viewing an ~87-km altitude that extended the cross-track FOV to ~900 km. A second aircraft, the DLR Falcon, participated in DEEPWAVE during the last half of the GV measurement interval. It hosted in situ dynamics and chemistry measurements and a downward-viewing aerosol Doppler lidar measuring line-of-sight winds below the Falcon, where aerosol backscatter was sufficient (see Table 2).

Ground-based DEEPWAVE measurements were likewise extensive (see Table 2). Radiosondes were launched at multiple sites, with those at three sites [two on the South Island (SI) western coast and one in the lee of the Southern Alps] providing frequent soundings during intensive observing periods (IOPs), and others launched from Tasmania and Macquarie Island coordinated with research flights (RFs) to support GW and predictability objectives in those regions. A 449-MHz wind profiler (WP) on the South Island western coast measured three-component winds continuously from ~0.5 to ~3–6 km. Additional instruments in the lee of the Southern Alps included 1) a ground-based AMTM measuring the horizontal temperature structure at ~87 km, 2) a Rayleigh lidar measuring temperatures from ~22 to 85 km, 3) two all-sky airglow imagers (ASIs) measuring airglow brightness at several altitudes from ~87 to 96 km, and 4) a Fabry–Perot interferometer (FPI) measuring winds and temperatures centered near ~87 and 96 km. For reference, the various airglow layers observed by the AMTMs, the ASIs, and the FPI all have full-width half maxima (FWHM) of ~7–10 km and may vary in altitude by several kilometers about their nominal

AFFILIATIONS: Fritts, B. P. Williams, Bossert, Mixa, Lieberman, and Laughman—GATS Inc., Boulder, Colorado; Smith, Kruse, Nugent, and Watson—Yale University, New Haven, Connecticut; Taylor, Pautet, and Criddle—Utah State University, Logan, Utah; Doyle, Reynolds, and Reinecke—Naval Research Laboratory, Monterey, California; Eckermann—Naval Research Laboratory, Washington, DC; Dörnbrack, Rapp, Kaifler, Wagner, and Gisinger—German Aerospace Center (DLR), Munich, Germany; Uddstrom, Revell, and Turner—NIWA, Newmarket, Auckland, New Zealand; Smith—Boston University, Boston, Massachusetts; Moore, Brown, Haggerty, Rockwell, Stossmeister, and S. F. Williams—Earth Observing Laboratory, National Center for Atmospheric Research, Boulder, Colorado; Hernandez*—University of Washington, Seattle, Washington; Murphy and Klekociuk—Australian Antarctic Division, Kingston, Tasmania, Australia; Reid—University of Adelaide, Adelaide, South Australia, Australia; Ma—Computational Physics, Inc., Springfield, Virginia
* Deceased
CORRESPONDING AUTHOR: D. C. Fritts, Boulder GATS Inc., 3360 Mitchell Lane, Boulder, CO 80301
E-mail: dave@gats-inc.com

The abstract for this article can be found in this issue, following the table of contents.
DOI:10.1175/BAMS-D-14-00269.1

In final form 19 May 2015

altitudes. A second Rayleigh lidar and a meteor radar measuring winds from ~80 to 100 km were deployed at Kingston, Tasmania. Ground-based instrument sites are shown in Fig. 1 (bottom). Figure 2 shows the extent of all DEEPWAVE measurements in altitude and latitude.

DEEPWAVE began with a test flight-planning exercise from 1 to 10 August 2013 to gain experience with forecasting and flight planning and to assess the reliability of such forecasts in preparation for the real field program. This effort, which is summarized and archived online (see appendix A), was judged to be quite successful and led to confidence in the utility of a suite of forecasts and ancillary satellite products in guiding DEEPWAVE IOPs and flight plans.

The DEEPWAVE field program was supported by an extensive operations center at Christchurch International Airport that coordinated all logistical and measurement activities (see appendix B). Forecasting and flight planning was supported by a suite of global, mesoscale, and regional models that proved to be highly valuable and often quite accurate on shorter time scales for final flight planning (see Table 3). These models are now being applied in concert with DEEPWAVE data analysis efforts to answer the science questions posed in Table 1. To aid DEEPWAVE research, a comprehensive DEEPWAVE data archive and management plan has been developed (see appendix A).

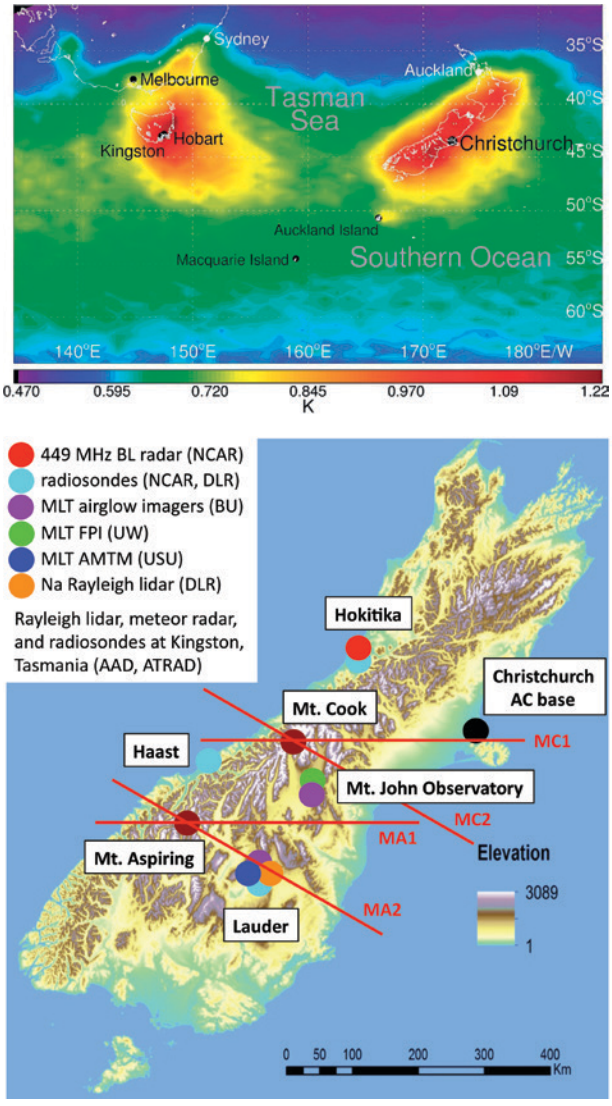

Fig. 1. (top) DEEPWAVE region of airborne and ground-based measurements over New Zealand, Tasmania, the Tasman Sea, and the Southern Ocean. Colors show the GW hotspots in AIRS rms temperature for Jun–Jul 2003–11 at 2.5 hPa. (bottom) Ground-based instruments contributing to DEEPWAVE in New Zealand and elsewhere (see legend). The major orographic features are Mt. Cook and Mt. Aspiring, and red lines show flight tracks MC1, MC2, MA1, and MA2, of which MC1 and MA2 were used for RF12 and RF22 measurements shown in Figs. 7, 9, and 10.

MOTIVATIONS. GWs, or buoyancy waves, for which the restoring force is due to negatively (positively) buoyant air for upward (downward) displacements, play major roles in atmospheric dynamics, spanning a wide range of spatial and temporal scales. Vertical and horizontal wavelengths, λ_z and λ_h, respectively, for vertically propagating GWs are dictated by their sources and propagation conditions and range from meters to hundreds and thousands of kilometers, respectively, with typical scales increasing by ~10 times or more from the troposphere to the MLT. Intrinsic frequencies (i.e., with respect to the local flow) vary from the inertial frequency to the buoyancy frequency. GWs at lower frequencies dominate the energy spectra, but higher-frequency GWs have larger vertical group velocities and contribute disproportionately to vertical transports of energy and momentum. As a result, smaller-scale GWs (λ_h ~ 10–200 km) have larger impacts on atmospheric circulation, weather, and climate, but their effects are much more challenging to quantify. GW influences typically increase with altitude because decreasing density implies increasing GW amplitudes and effects. Large GW amplitudes drive nonlinear (NL) wave–wave and wave–mean flow interactions, instabilities, turbulence, and energy and momentum deposition that result in a strong evolution of the GW spectrum with altitude. These complex dynamics, and their significant dependence on GW sources and the environments through which they propagate, pose major challenges for their parameterizations in global weather and climate models.

Table 2. Instruments and capabilities.

Instrument	Variable	Altitude
GV instruments		
Avionics/GPS	(x, y, z), (U, V, W)	FL
Gust probe	u, v, w at 25 Hz	FL
279 dropsondes	$V_h(z)$, $q(z)$, $T(z)$	FL–ground
MTP	$T(z)$	FL ± ~5 km
Rayleigh lidar	$\rho(z)$, $T(z)$	~20–60+ km
Na resonance lidar	$\rho_{Na}(z)$, $T(z)$	~75–100 km
AMTM	$T(x, y)$, zenith	~87 km
Airglow cameras	$I(x, y)$, side views	~87 km
Falcon instruments		
Avionics/GPS	(x, y, z), (U, V, W)	FL
Gust probe	u, v, w at 25 Hz	FL
Doppler lidar	$u(x, z)$, $w(x, z)$	~0–10 km
Ground-based instruments		
WP: Hokitika	$(U, V, W)(z)$	~0–4 km
Radiosondes: Haast (51), Hokitika (145), Lauder (98), and at Hobart and South Islands	$V_h(z)$, $T(z)$, $q(z)$	~0–30 km
Rayleigh lidars: Lauder and Kingston	$\rho(z)$, $T(z)$	~20–70 km
AMTM: Lauder	$T(x, y)$	~87 km
ASIs: Lauder and MJO	$I(x, y)$ all sky	~87–96 km
FPI: MJO	V_h, T	~87, 96 km
Meteor radar: Kingston	$V_h(z)$	~80–100 km

Scientific interests and societal needs have motivated many previous studies of GWs from the stable boundary layer and troposphere, through the stratosphere and mesosphere, and into the thermosphere. Among the more important of these are the following:

1) GWs pose hazards to people and property; examples include sometimes severe downslope winds and severe turbulence at airline flight altitudes;
2) GWs exhibit a wide range of dynamics and effects that play important roles in atmospheric weather and climate from the surface into the MLT, but many of these are poorly understood at present;
3) GW motions are incompletely resolved both in global satellite observations and in global numerical weather prediction (NWP) and climate models, and so their effects in large-scale weather and climate models must be parameterized; and
4) Inadequate understanding and characterization of GW dynamics and effects have resulted in parameterizations of their effects in NWP and climate models that are acknowledged to have major deficiencies.

The importance of GWs in multiple atmospheric processes has led to thousands of papers dealing with diverse GW topics including 1) sources; 2) propagation and refraction in variable environments; 3) linear and nonlinear behavior; 4) wave–wave and wave–mean flow interactions; 5) instabilities and turbulence due to large GW amplitudes and superpositions; 6) energy, momentum, and tracer transports; 7) parameterizations of GW effects in large-scale (LS) models; and 8) GW influences on other processes such as convection, cloud microphysics, chemical reactions, and plasma dynamics and instabilities in the ionosphere. Many other papers have addressed important GW roles in oceans, lakes, other planetary atmospheres, and stellar interiors.

PREVIOUS RESEARCH. The scope of GW dynamics and roles is reflected in the many seminal papers, reviews, and books describing these various

Table 3. Forecasting and research models. FV = finite volume. DNS = direct numerical simulation and NCEP GFS = National Centers for Environmental Prediction Global Forecast System.

Model	Type, application	Horizontal Resolution		Altitudes
		Operational/ real time	Research	
ECMWF IFS	Global, FC	TL1239 (~16 km)		0–80 km
NCEP GFS	Global, FC	T574 (~23 km)		0–65 km
NIWA/UKMO UM	Global, FC	N768 (~17 km)		0–80 km
NAVGEM	Global, FC, RE	T359 (~37 km)	T119–T425 (~30–110 km)	0–70 km
COAMPS adjoint	Regional, FC, RE	35 km	5–35 km	0–30 km
COAMPS	Regional, FC, RE	5 and 15 km	1–15 km	0–50 km
NZ Limited Area Model (NZLAM)	Regional, FC	12 km		0–80 km
NZ Convective Scale Model (NZCSM)	Regional, FC	1.5 km		0–40 km
WRF (various)	Regional, FC, RE	6 km	2 km	0–45 km
FR linear	Local, FC, RE	0.5–1 km	any	0–100 km
FV DNS	Local, RE		20 m–1 km	0–400 km
Spectral DNS	Local, RE		1–10 m	0–10 km

processes. Examples of those addressing atmospheric GW topics of most relevance to DEEPWAVE science include the following:

1) GW linear dynamics, propagation, conservation properties, and fluxes (Hines 1960; Eliassen and Palm 1961; Bretherton 1969a,b; Booker and Bretherton 1967; Gossard and Hooke 1975; Smith 1980; Nappo 2013);
2) GW sources, characteristics, and responses (Fritts 1984; Fritts and Alexander 2003);
3) GW refraction, mean flow interactions, and responses (Lindzen and Holton 1968; Holton 1982; Garcia and Solomon 1985; Haynes et al. 1991; Sutherland 2010; Bühler 2014);
4) GW spectral properties, interactions, instabilities, and saturation (Yeh and Liu 1981; Smith et al. 1987; Hines 1991; Lombard and Riley 1996; Sonmor and Klaassen 1997; Fritts et al. 2009); and
5) GW parameterizations for NWP and climate models (Lindzen 1981; Holton 1982; McFarlane 1987; Warner and McIntyre 1996; Hines 1997a,b; Kim et al. 2003; Fritts and Alexander 2003).

Below we provide an overview of previous research on atmospheric GWs, focusing on airborne measurement programs, but also noting contributions by other ground-based, in situ, and satellite measurements (a number of which were employed during DEEPWAVE). Numerous modeling studies have likewise addressed GW sources, propagation, linear and nonlinear dynamics, and their various effects. However, we will restrict our overview to those

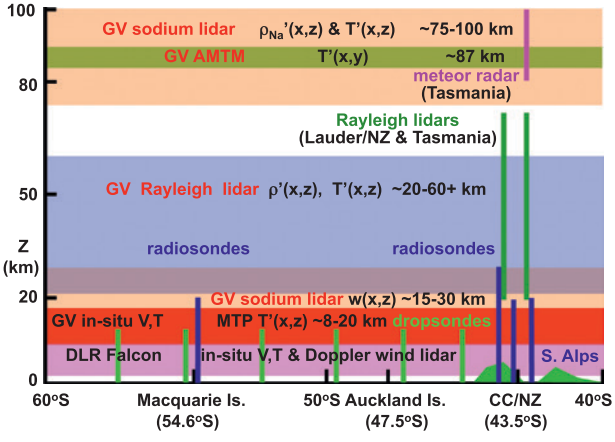

Fig. 2. North–south cross section showing the types of airborne and ground-based instruments contributing to DEEPWAVE measurements and their coverage in latitude and altitude.

efforts performed specifically for comparisons with observational data or which offer a global perspective on resolved GW sources, propagation, and effects.

The earliest studies of mountain waves (MWs) in the 1930s employed balloons and gliders to sample MW flows in North Africa and Europe (e.g., Queney 1936a,b; Küttner 1938, 1939; Manley 1945). These observations provided key insights into the structure of MWs and lee waves and, together with the Sierra Wave Project (see below), motivated initial theoretical advances (e.g., Queney 1947; Scorer 1949; Long 1953, 1955; see also Grubišić and Lewis 2004). Other observations of plasma motions in the ionosphere (now called traveling ionospheric disturbances) motivated the seminal paper by Hines (1960) that provided the theoretical framework for GW propagation throughout the atmosphere. Brief overviews of subsequent GW research using ground-based, in situ, and satellite measurements, accompanying more recent airborne programs, and employing mesoscale and global modeling are provided below.

Ground-based, in situ, and satellite measurements. Ground-based and in situ measurement capabilities have improved dramatically since the earliest MW studies. Radiosondes have provided evidence of GW sources, scales, amplitudes, intrinsic properties, and fluxes from the surface into the middle stratosphere for many years (e.g., Tsuda et al. 1994; Allen and Vincent 1995; Sato and Dunkerton 1997; Sato and Yoshiki 2008; Geller et al. 2013). Stratospheric superpressure balloon measurements have likewise defined GW intrinsic properties and momentum fluxes (MFs) in the lower stratosphere and, in particular, their intermittency and potential for infrequent, but very strong, GW events to contribute a large fraction of the total momentum flux (e.g., Hertzog et al. 2008; Plougonven et al. 2008, 2013). Rocketborne falling spheres and newer ionization gauges, lidars, and other probes have measured winds, temperatures, and turbulence from ~30 to 100 km and enabled studies of energy dissipation rates due to GW breaking, MW filtering during a stratospheric warming, and anomalous MLT mean structure accompanying strong planetary waves (PWs) in the Southern Hemisphere and other dynamics (e.g., Rapp et al. 2004; Wang et al. 2006; Goldberg et al. 2006).

Multiple types of radars have quantified GW amplitudes, scales, spectral character, momentum fluxes, and evidence of various interaction and instability processes from the troposphere to the MLT for about five decades (e.g., Gossard et al. 1970; Atlas et al. 1970; Woodman and Guillen 1974; Sato and Woodman 1982; Vincent and Reid 1983; Balsley and Garello 1985; Fritts and Rastogi 1985; Fritts and Vincent 1987; Smith et al. 1987; Tsuda et al. 1989, 1990; Sato 1994; Thomas et al. 1999; Pavelin et al. 2001; Luce et al. 2008). Rayleigh and resonance lidars have likewise contributed to the definition of GW properties via measurements of temperatures, winds, and/or metallic species densities from very low altitudes to ~100 km or above (e.g., Chanin and Hauchecorne 1981; Gardner and Voelz 1987; She et al. 1991; Whiteway and Carswell 1994; Williams et al. 2006; Duck et al. 2001; Alexander et al. 2011; Lu et al. 2015). Other optical instruments, especially ASIs and the newer AMTMs, provide valuable information on GW horizontal wavelengths, orientations, phase speeds, and amplitudes, sometimes at multiple altitudes, that contribute greatly to quantification of GW character, propagation, and potential for instability and mean flow interactions (e.g., Gavrilov and Shved 1982; Taylor et al. 1995; Taylor and Hapgood 1988; Hecht et al. 1997, 2001; Walterscheid et al. 1999; Nakamura et al. 2003; Smith et al. 2009; Pautet et al. 2014; Hecht et al. 2014; Fritts et al. 2014).

Multi-instrument measurement programs performed at facilities having extensive ground-based instrument capabilities, such as those that often accompany large radar and/or rocket facilities, have made especially valuable contributions to GW studies. This is because no single instrument can define all of the atmospheric properties and spatial and temporal variability needed to fully quantify the local GW field. Examples of these facilities include the Arctic Lidar Observatory for Middle Atmosphere Research in Norway (69.3°N); the Poker Flat Research Range in Alaska (65.1°N); the Bear Lake Observatory in Utah (42°N); the middle- and upper-atmosphere (MU) radar in Japan (34.9°N); the National Atmospheric Research Laboratory in India (13.5°N); the Equatorial Atmosphere Radar (EAR) in Indonesia (0°); the Jicamarca Radio Observatory in Peru (12°S); the Andes Lidar Observatory in Chile (30.2°S); Buckland Park in Australia (35°S); the Davis (Australia) and Syowa (Japan) Antarctic stations (68.6° and 69°S, respectively); and additional facilities having valuable correlative instrument capabilities in Antarctica, Argentina, Australia, Brazil, Canada, China, France, Germany, India, Puerto Rico, Sweden, and elsewhere.

Measurements of radiances and inferred temperatures by multiple satellite instruments employing limb, sublimb, and nadir viewing have been used to estimate GW temperature variances and momentum fluxes from the lower stratosphere into the MLT for many years. These have provided enticing insights into GWs arising from various sources. In many

cases, however, satellite measurements exhibit strong observational constraints because of line-of-sight averaging or weighting-function depths comparable to, or greater than, the smaller, but important, GW scales. Such measurements nevertheless reveal the larger-scale responses to multiple sources, define the global hotspots of GW activity and their seasonal variations, and on occasion capture very strong GW responses under ideal viewing conditions (e.g., Dewan et al. 1998; Eckermann and Preusse 1999; Ern et al. 2004; Eckermann et al. 2007; Wu and Eckermann 2008; Alexander et al. 2009, 2010; Eckermann and Wu 2012; Geller et al. 2013; Hendricks et al. 2014). Figure 3 shows the measurement capabilities of various satellite viewing geometries compared to DEEPWAVE and the GW wavelengths expected to account for the major GW momentum fluxes. Nadir measurements [e.g., Atmospheric Infrared Sounder (AIRS)] extend to relatively small GW λ_h, but these often fail to capture the smaller-λ_h GW responses inferred to contribute the largest local momentum fluxes (Fritts et al. 2002, 2014; Hertzog et al. 2012). Nadir measurements also often fail to capture larger-λ_h GWs when the GW λ_z is comparable to or smaller than the depth of the weighting function (e.g., Eckermann et al. 2009; Gong et al. 2012).

More recent airborne measurement programs. The next significant airborne measurement program following those in the 1930s was the Sierra Wave Project. This project employed two gliders in 1951/52 and two gliders and two powered aircraft in 1955, together with radiosondes and ground measurements, and yielded a significantly improved understanding of MW structure and related theoretical advances (Grubišić and Lewis 2004). Subsequent MW and lee-wave studies over the Rockies in the 1960s and 1970s used improved instrumentation aboard various aircraft to sample the MW, lee wave, and turbulence environments accompanying MW breaking. These provided more complete descriptions of the flow structures and evolutions and motivated initial modeling of these events (e.g., Kuettner and Lilly 1968; Lilly and Kennedy 1973; Brinkmann 1974; Clark and Peltier 1977; Lilly 1978; Klemp and Lilly 1978; Lilly et al. 1982).

More recent MW airborne studies benefitted from further expanded measurement capabilities, including dropsondes, GPS positioning, and/or the MTP, ground-based instruments, and associated modeling, for example, over the Welsh mountains (Whiteway et al. 2003); over the Alps during the Alpine Experiment (ALPEX), Pyrénées Experiment (PYREX), and Mesoscale Alpine Programme (MAP)

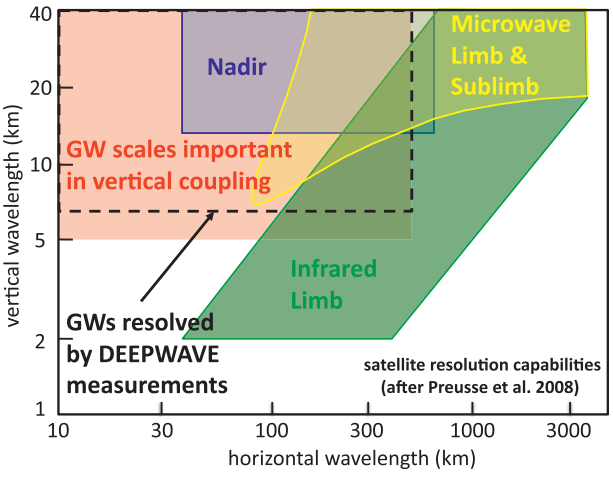

Fig. 3. Schematic of the sensitivity of various satellite measurement techniques to GW horizontal and vertical wavelengths (after Preusse et al. 2008) relative to the GW scales expected to contribute most to GW momentum fluxes throughout the atmosphere (pink). The instrument categories include microwave limb and sublimb (e.g., MLS), infrared limb [e.g., High Resolution Dynamics Limb Sounder (HIRDLS) and SABER], and nadir [e.g., AIRS and Advanced Microwave Sounding Unit (AMSU)]. The range of scales resolved by GV lidars (dashed line) is determined by the altitude coverage of each lidar separately (~30–40 km) and together (~80 km), the length of individual flight segments (~500–2000 km), and the minimum temporal and vertical averaging required for a particular measurement.

(e.g., Bougeault et al. 1990, 2001; Smith et al. 2002; Doyle and Smith 2003; Doyle and Jiang 2006); over the Sierra Nevada during the Terrain-Induced Rotor Experiment (T-REX) (e.g., Grubišić et al. 2008; Smith et al. 2008; Doyle et al. 2011); and elsewhere (e.g., Brown 1983; Whiteway et al. 2003; Doyle et al. 2005). Additional airborne studies explored the influences of MWs on the formation of polar stratospheric clouds at Arctic and Antarctic latitudes (e.g., Carslaw et al. 1998; Eckermann et al. 2006b).

Other airborne programs targeted more general GW responses. The Global Atmospheric Sampling Program (GASP) employed commercial aircraft for global in situ measurements that enabled comparisons of GW responses to various sources (e.g., Nastrom and Fritts 1992; Fritts and Nastrom 1992). The Airborne Lidar and Observations of Hawaiian Airglow 1990 (ALOHA-90) and the Airborne Lidar and Observations of Hawaiian Airglow/Arctic Noctilucent Cloud Campaign 1993 (ALOHA/ANLC-93) measurement programs employed a lidar and ASI to sample GWs extending from the stratosphere into the MLT (Hostetler et al. 1991; Hostetler and Gardner 1994; Swenson et al. 1995). Several airborne measurements

Table 4. IOP and research flight focuses and summaries. TW = trailing wave, PF = predictability flight, FL = flight level, SI = South Island, CW = convective waves, FWs = frontal waves, SO = Southern Ocean.

IOP	RF	Date	Primary/secondary targets	Flight summary
1	1	6 Jun	MWs/TWs/PF	Weak GWs/sources expected/verified
2	2	11 Jun	MWs, Tasmania	Weak FL GWs, large amplitudes in MLT
3	3	13 Jun	PF, Tasman Sea	Successful PF
	4	14 Jun	MWs/TWs SI MA2	MWs/TWs at FL, MLT MWs
4	5	16 Jun	MWs/TWs SI MC2	Weak MWs at FL, in stratification and MLT
5	6	18 Jun	MWs over Tasmania	Weak FL responses, possible MWs in MLT
6	7	19 Jun	MWs/CWs/FWs, eastern ocean	Significant/diverse FL/MLT GW activity
7	8	20 Jun	MWs/TWs SI MA1	Weak MWs, FL and MLT
8	9	24 Jun	PF Tasman Sea, MC2	PF, FL MW breaking/turbulence in MLT
	10	25 Jun	MWs/TWs SI MC2	Significant MWs, MLT MWs/CWs
9	11	28 Jun	PF Tasman Sea, SI MC2	CWs, jet stream GWs, MLT GWs/MWs
	12	29 Jun	MWs/TWs SI MC2/MA2	Strong MWs/breaking, MWs in MLT
	F1	30 Jun	MWs SI MA2	Strong, transient MWs; immediately after RF12
	13	30 Jun	MWs/TWs SI MC2/MA2	Similar to RF12, MWs and GWs in MLT
	F2	30 Jun	MWs SI MA2	As for F1, but weaker MWs
	14	1 Jul	MWs/TWs SI MC1	Weak FL MWs, stronger in MLT
CF	F3	2 Jul	Tropopause fold over SI	Moderate GWs near the jet and tropical fold
	15	3 Jul	Lee of SI	Daytime flight, FL measurements only
10	F4	4 Jul	MWs SI MA1	Strong MWs; immediately before RF16
	16	4 Jul	MWs/TWs SI MA1	Largest FL MWs, also MLT MWs
	F5	4 Jul	MWs/TWs SI MA1	Strong MWs; together with RF16
11	17	5 Jul	SO waves (east and south)	Large-scale, large-amplitude GWs in MLT
12	18	7 Jul	PF SO/Tasman Sea	Good jet stream FL and MLT GWs
	19	8 Jul	SO waves	Large-scale, large-amplitude GWs in MLT
13	20	10 Jul	PF/MWs SO SI MC2	Joint with F6, significant MLT GWs
	F6	10 Jul	Intercomparison flight with RF20	Ongoing analysis
	F7	11 Jul	MWs SI MC2	Moderate MWs
	21	11 Jul	MWs/TWs SI MC2	With F7 and F8, FL and MLT MW responses
	F8	11 Jul	MWs SI MC2	Moderate MWs
	F9	12 Jul	MWs SI MC2 and north	Varying/moderate GW responses over SI
	F10	13 Jul	MWs SI MC2 and north	Varying/moderate GW responses over SI
	22	13 Jul	MWs SI MC1	Large-scale/amplitude GWs/MWs in MLT
14	23	14 Jul	SO/island waves	Strong/variable MLT MWs Auckland Island
	24	15 Jul	SO/island waves	Significant GWs in AIRS and MLT
15	F12	16 Jul	MWs SI MC2 and north	Weak MWs, FL and MLT
16	25	18 Jul	SO waves	Strong SI GWs, SO GWs AIRS/MLT
	26	20 Jul	MWs SI along mountains	Weak FL GWs, strong AIRS and MLT
	F13	20 Jul	MWs SI along mountains	Moderate FL GWs; after RF26

also provided evidence of GWs generated by deep convection and their momentum fluxes at flight altitudes (e.g., Kuettner et al. 1987; Pfister et al. 1993; Alexander and Pfister 1995).

Mesoscale and global modeling of GWs. Modeling capabilities for mesoscale and global GW studies have improved dramatically in recent years because of ever-increasing computational resources. As a result, various models have been employed in support of GW measurement programs and to identify GW sources and key dynamics spanning larger spatial scales. Mesoscale models have aided the interpretation of MAP, T-REX, and other airborne MW programs, been employed for intermodel comparisons for several events (e.g., Dörnbrack et al. 2001; Smith et al. 2002; Doyle and Smith 2003; Doyle and Jiang 2006; Doyle et al. 2000, 2011), and assessed the dynamical responses and resolution dependence of airflow over small islands (e.g., Vosper 2015). Global forecast and research models (REs) now achieve spatial resolutions of ~25 km or better that enable direct modeling, rather than parameterization, of GWs extending to horizontal scales as small as ~100 km. As examples, Yamashita et al. (2010) showed that the European Centre for Medium-Range Weather Forecasts (ECMWF) T799 model described GWs having λ_x > 100 km that agreed reasonably with a much higher-resolution Weather Research and Forecasting (WRF) Model simulation and AIRS observations of GWs due to a typhoon, exhibited similar GW variance distributions as the Microwave Limb Sounder (MLS), but underestimated GW amplitudes by ~2 times compared to Sounding of the Atmosphere using Broadband Emission Radiometry (SABER) measurements. Shutts and Vosper (2011) employed the Met Office (UKMO) and ECMWF global models and a very-high-resolution (4 km) unified model to examine the MW energy and momentum fluxes over the southern Andes. They found a peak in the fluxes at λ_x ~ 400 km, with approximately half the fluxes at λ_x < 200 km. Sato et al. (2012) used a high-resolution middle-atmosphere general circulation model (GCM) to explore the stratospheric dynamics of MWs having λ_x ~ 200 km and larger arising from the southern Andes. They found that the MWs refract strongly into the polar vortex because of horizontal wind shears and yield downward-propagating responses below ~40 km because of nonlinear dynamics at higher altitudes. Similar improvements in characterization of MW and more general GW influences at higher spatial resolution were also found to occur in the Community Atmosphere Model, version 4.0 (CAM4), and the Whole Atmosphere Community Climate Model (WACCM) (Bacmeister et al. 2014; Liu et al. 2014).

FIELD PROGRAM AND EPO OVERVIEW.

The DEEPWAVE field program was complex and was made possible by the participation of a large number of individuals from the NSF principal investigator (PI) teams, NCAR, Naval Research Laboratory (NRL), DLR, National Institute of Water and Atmosphere Research (NIWA), Australian Antarctic Division (AAD), and other colleagues and students in New

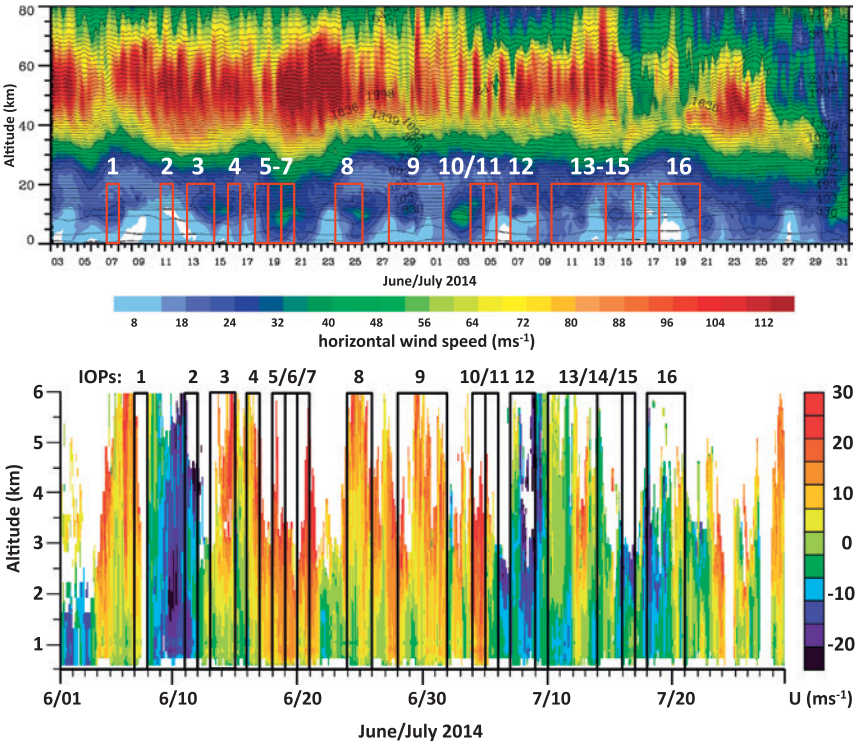

Fig. 4. DEEPWAVE IOPs (red rectangles with white labels) shown with respect to (top) the large-scale ECMWF horizontal winds and potential temperatures (contours) and (bottom) the Hokitika WP eastward 6-h mean winds throughout the DEEPWAVE field program.

Table 5. GB–IOP (no coincident RF) Lauder lidar/AMTM GW summaries. *T'* = temperature fluctuations, MF = momentum flux, *I'* = intensity fluctuations, and SS = small scale.

GB–IOP	Date	GW responses, MW forcing, and large-scale influences
GB1	30 May	~20–60-km MWs and other GWs, apparent correlation with *T*
GB2	31 May	Slow ~60-km GWs with strong, sharp "front" and cooling/brightening
GB3	1 Jun	MWs ~80 km moderated by larger-scale wave with large *T'*, *U'* ~ 10 m s^{-1}
GB4	2 Jun	Very strong MWs ~ 15–80 km, large MFs, little evidence of instabilities
GB5	11 Jun	Apparent bore or NL wave train with sharp *T* increase thereafter
GB6	12 Jun	Strange behavior in MLT
GB7	15 Jun	Strong AMTM *I'* and *T'* modulation in MLT
GB8	18 Jun	MWs and other responses in MLT
GB9	19 Jun	Lots of MLT GWs, MWs not dominant—coordinate with RF7
GB10	21 Jun	Very strong MWs ~ 15–80 km, large MFs, instabilities, weak MW forcing
GB11	22 Jun	Lots of GW responses, multiple SS events in MLT
GB12	23 Jun	Lots of GW responses, multiple SS events in MLT
GB13	26 Jun	Large linear/nonlinear MWs, SS instabilities in MLT
GB14	28 Jun	Strong SS MWs and instabilities in MLT
GB15	4 Jul	Strong complex GWs in MLT, mostly westward propagation
GB16	10 Jul	Large-amplitude, transient SS MWs ~ 10–100 km, very large SS MFs
GB17	14 Jul	Large-amplitude, transient SS MWs ~ 30–40 km, very large MFs, northwest–southeast alignment
GB18	16 Jul	Significant SS GW activity, some MWs
GB19	17 Jul	Strong, coherent, sustained SS MWs ~ 20–30 km, north-northwest–south-southeast alignment
GB20	18 Jul	Significant, persistent SS and LS MWs, north-northwest–south-southeast alignment
GB21	31 Jul–2 Aug	Very large MW event in Lauder–Rayleigh lidar observations
GB22	14–15 Aug	Very large MW event in Lauder–Rayleigh lidar observations

Zealand, Australia, and Austria. Altogether, over 100 people contributed to various aspects of the program. DEEPWAVE participants and their roles are listed in appendix D. The various tasks included aircraft logistics, operations and maintenance, ground-based instrument installations, weather forecasting and updates, flight planning and debriefs, personnel scheduling, education and public outreach (EPO) activities, and local outreach. Most activities were performed during daytime, but, because of the extensive use of the new GV lidars and imagers, most research flights and all ground-based optical measurements were performed at night. The major components of the program are discussed further below.

Weather forecasting, briefings, and updates. Daily weather forecasting began each morning, with efforts coordinated by a lead forecaster and contributed to by a team including scientists, students, and NIWA staff using local weather observations and forecasts and mesoscale and global forecast models (FCs; see Table 3). The forecast models often proved to be quite accurate on short time scales and hence very valuable for these purposes. The focus was on events having GW responses expected to penetrate into the stratosphere and MLT and weather impacting GV operations. Weather briefings occurred each day at 1300 local time (LT) [0100 univeral time (UT)] and typically reviewed the weather for that day (if there was a research flight scheduled) and 1–3 days out for flight planning purposes. On days having research flights scheduled, an additional weather update was also provided ~2 h before flight departure.

Flight planning. Flight planning typically involved submission of flight proposals by individuals or teams designed to address specific DEEPWAVE science questions. Occasionally, flight plans looked farther ahead and anticipated a combination of flights, for example, predictability and verification or successive

sampling of a multiday event. Often, alternative flight proposals were merged to optimize the expected results and/or address common measurement goals. A subcommittee of scientists that changed weekly determined the final flight plan in the event of competing proposals. The selected flight plan was then sent to the Earth Observing Laboratory (EOL) team for review and feedback.

Research flights and large-scale context. All research flights [RFs and Falcon research flights (FFs)] for the GV and the Falcon were part of an IOP ranging from 1 to 4 days to facilitate coordination with ground-based measurements. GV flight durations ranged up to ~9 h and flight distances ranged up to ~8,000 km. Falcon flights had maximum durations and lengths of ~3.5 h and ~3,000 km, respectively. The large majority of RFs and FFs were performed at high altitudes, ~12–13.7 km for the GV and ~10–11 km for the Falcon. For the GV, this was done for fuel efficiency and because the GV lidars were not allowed to operate at lower altitudes. Both aircraft also performed a number of flight segments at lower altitudes to sample interesting events on various occasions. MW flights targeted strong and weak forcing to span a range of responses at higher altitudes. The IOPs, dates, research targets, and flight summaries for all RFs flown during DEEPWAVE are listed in Table 4.

IOPs are shown in the context of the large-scale ECMWF horizontal winds from 0 to 80 km in Fig. 4 (top). The dominant feature is the polar night jet with a maximum wind often exceeding 100 m s^{-1} at ~50–60 km that is presumably modulated in strength by PWs on time scales of ~5–10 days. The poleward jet associated with frontal systems exhibits episodic maxima of ~30–50 m s^{-1} at ~8–12 km on similar time scales. Also seen in the second half of July are two intervals in which the polar night jet decreases, first to ~60 m s^{-1} (~15–20 July) and then to ~30 m s^{-1} (beginning ~29 July). These intervals accompany significant enhancements in the zonal wavenumber 1-PW amplitude that yield both a weak stratospheric warming and westward wind perturbations that account for the weaker ECMWF winds at these times.

Ground-based measurements. As noted above, DEEPWAVE was supported by extensive ground-based measurements. The WP operated continuously

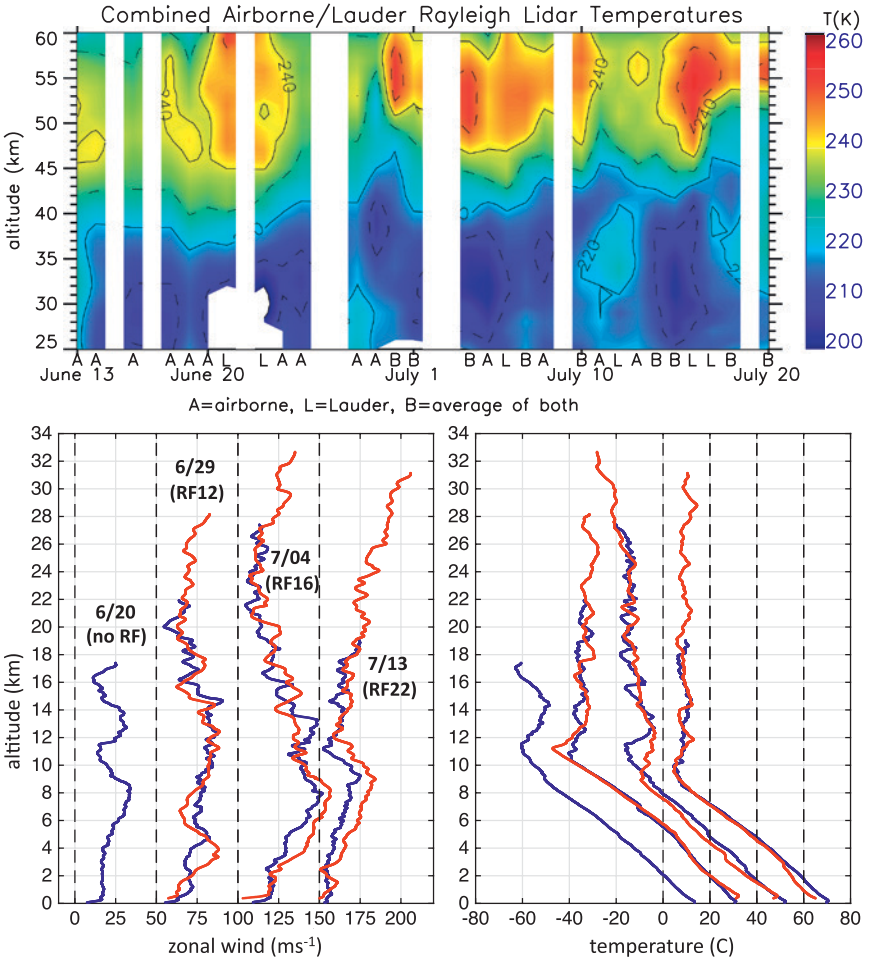

Fig. 5. (bottom) Radiosonde zonal wind and temperature profiles at Hokitika (blue) and Lauder (red) at 2307 UT 20 Jun (as best available data for 21 Jun), 1053 and 1129 UT 29 Jun (RF7), 1403 and 1440 UT 4 Jul (RF16), and 1059 and 0238 UT 13 Jul (RF22), respectively. (top) RF-mean and/or nightly mean temperatures obtained with the GV airborne and Lauder ground-based Rayleigh lidars from 13 Jun to 20 Jul that reveal the variability of mean temperatures and atmospheric stability over South Island during DEEPWAVE. Note the code at bottom that specifies which lidar(s) contributed each day. Winds and temperatures on successive days are offset by 50 m s^{-1} and 20°C, respectively.

from 28 May to 28 July. Radiosondes were launched daily at Hokitika from 24 May to 18 July, at Lauder from 13 June to 1 August, at a higher cadence during IOPs at these sites and at Haast, and at Hobart and Macquarie Island to support flights or predictability objectives in those areas. The AMTM, ASIs, and FPI at Lauder and Mt. John Observatory (MJO) performed routine nighttime observations spanning the DEEPWAVE core measurement interval. The DLR lidar at Lauder operated from 19 June to 6 November. The Kingston lidar operated in coordination with GV flights over Tasmania and the Tasman Sea, and the meteor radar at Kingston operated continuously beginning 10 June. The altitudes sampled by these various instruments are shown with vertical bars in Fig. 2. Additional ground-based IOPs were designated on nights for which interesting responses were observed that correlated with the forecast models and measurements at lower altitudes. These events are listed in Table 5.

Four examples of radiosonde measurements at Hokitika and Lauder relevant to specific cases discussed further below are shown in Fig. 5 (bottom). Shown in Fig. 5 (top) are RF-mean or nightly mean temperatures obtained with the GV airborne and Lauder Rayleigh lidars for each available measurement over South Island. These illustrate some of the diversity of GW propagation environments from the surface to 60 km during the DEEPWAVE program.

EPO activities. DEEPWAVE EPO efforts had two primary objectives: 1) to increase the awareness of students in kindergarten–grade 12 of the field of atmospheric science by exposing them to research methods through engaging presentations and interactions with early-career scientists and 2) to increase public awareness of the DEEPWAVE science objectives and societal benefits on an international level. The program consisted of targeted student enrichment activities including 10 presentations to 565 middle and high school students; Internet-based outreach efforts that included 11 educational web pages with 2,000 views in a 104-day period, 15 Facebook posts, blog posts, and tweets from postdoctoral scholars in the field; a research aircraft public open house with over 250 visitors; media visits resulting in several high-profile pieces broadcast in New Zealand; and various printed information. Additionally, 26 undergraduate and graduate (grad) students from eight organizations and universities were directly involved with DEEPWAVE research and operations, gaining valuable experience in observational fieldwork.

INITIAL MEASUREMENTS AND RESULTS.

Initial DEEPWAVE data analysis efforts are addressing

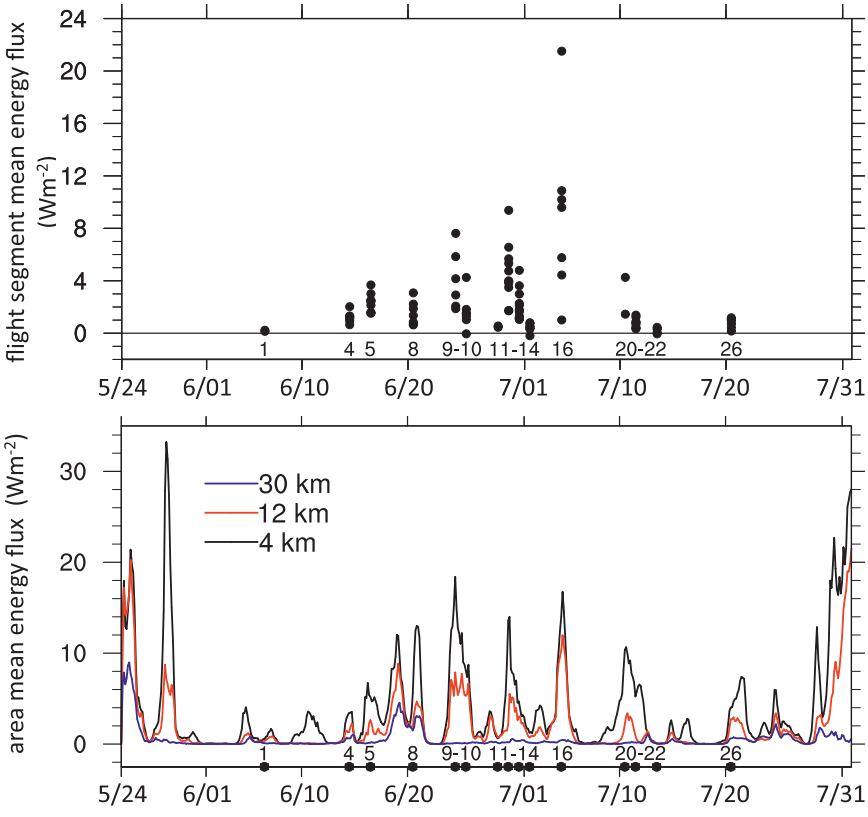

Fig. 6. (top) Flight-level vertical energy fluxes ⟨*p*′*w*′⟩ computed for each GV MW flight segment over South Island throughout the DEEPWAVE field program. Note the large variability accompanying the largest RF mean energy fluxes and largest-amplitude MWs. (bottom) Regional vertical energy fluxes over South Island computed from WRF constrained by ECMWF IFS initial conditions at 4, 12, and 30 km as a guide to MW dissipation with altitude due to variable MW forcing and environments. Numerical designations along the *x* axis in the bottom panel show the RFs for which GV flight-level energy fluxes are displayed in the top panel.

a number of topics and yielding a variety of tantalizing results. Example "first results" that will be discussed briefly below include 1) strong variability of MW energy fluxes among, and within, the various MW flights; 2) evidence of MW breaking at flight altitudes; 3) predictability targeting and influences; 4) MWs arising from weak forcing attaining large amplitudes at higher altitudes; 5) strong three-dimensional (3D) MW responses at high altitudes over Auckland Island; 6) GWs in the stratosphere apparently generated within the jet stream; 7) responses to weak MW forcing over several days that yielded intermittent MW breaking in the MLT; and 8) comparisons of DEEPWAVE measurements with model forecasts and AIRS temperature observations.

MW flight-level responses and predictability. An initial assessment of MW propagation employing GV flight-level (FL) MW energy flux estimates $\langle p'w' \rangle$ (where p' and w' are the in situ GV measurements of pressure and vertical velocity perturbations, and brackets denote horizontal averaging) for each MW RF is shown in Fig. 6 (top). WRF Model estimates of these fluxes at 4, 12, and 30 km for initial conditions specified by the ECMWF Integrated Forecasting System (IFS) model are shown in Fig. 6 (bottom) and were computed following Kruse and Smith (2015). The WRF GW energy flux maxima typically accompany frontal systems that bring strong lower-level flow over South Island. RF energy fluxes are positive (negative) for upward (downward) MW propagation, suggesting strong variability in MW strength and propagation within individual MW events. Modeled energy fluxes suggest variable MW propagation and dissipation at higher altitudes depending on the MW forcing strengths and propagation environments. The numbered circles on the x axis in Fig. 6 (bottom) are the RFs for which computed energy fluxes are shown in the top panel.

One of the strongest MW events during DEEPWAVE occurred during RF12 on 29 June. The GV flew a box pattern with repeated flight segments over Mt. Aspiring and Mt. Cook. Data from segments 14 and 22 along Mt. Aspiring flight-track 2 (MA2; see Fig. 1) are shown in Fig. 7. Most notable are the very different responses separated by only 1.5 km in altitude. At 12.2 km, the along-track wind accelerated to 25 m s^{-1} and then decelerated to 12 m s^{-1} over the high terrain. At 13.7 km, the disturbance was stronger and decelerated to ~0 m s^{-1}, which is expected to accompany wave breaking. The vertical velocity fields (top panel) were also different at the two levels. At 12.2 km, these mostly showed a quasi-periodic train of small-scale (SS) waves downwind of the highest orography. These were likely trapped waves having small energy and momentum fluxes. At 13.7 km, a burst of high-frequency turbulence occurred over the high terrain, likely accompanying wave breaking.

An example of the predictability component of DEEPWAVE is illustrated in Fig. 8 for 13 June 2014 (RF3). The Coupled Ocean–Atmosphere Mesoscale Prediction System (COAMPS) forecast and adjoint models (Amerault et al. 2008; Doyle et al. 2014) were used to compute the forecast sensitivity to the initial state, and these regions of high sensitivity were targeted for additional dropwindsonde (DWS) observations. As an example, the color shading in the Tasman Sea (Fig. 8a) highlights the upstream regions where the 24-h COAMPS forecast kinetic energy in the lowest 1 km above the surface in the gray box is most sensitive to the initial-state 700-hPa u-wind

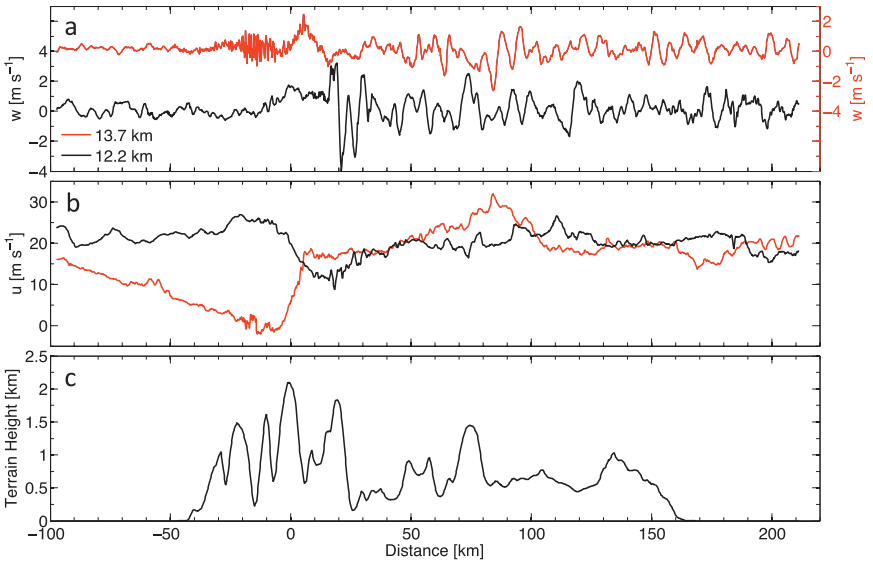

Fig. 7. GV flight-level gust-probe data from RF12 on 29 Jun. Two flight segments over Mt. Aspiring along MA2 (see Fig. 1) are shown: segment 14 at z = 12.2 km (black) and segment 22 at z = 13.7 km (red). Shown are (a) vertical velocities, (b) along-track cross-mountain wind speed, and (c) terrain height. Note that the GV passed through a region of MW breaking on segment 22 where the MW velocity exactly cancelled the along-track mean wind.

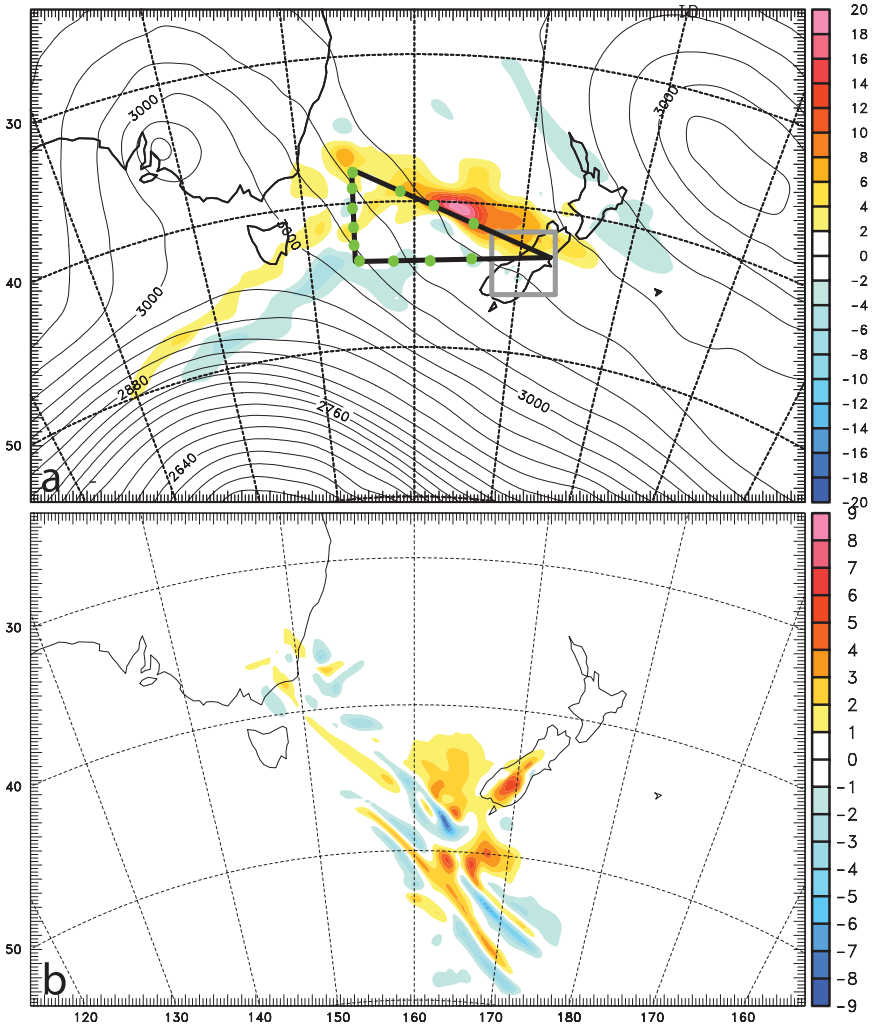

Fig. 8. (a) The sensitivity of the 24-h COAMPS forecast kinetic energy in the lowest 1 km above the surface (gray box) to the initial-state 700-hPa *U*-wind component at 0600 UTC 13 Jun 2014 (color scale with interval of 2 × 10^{-3} m s^{-1}). (b) The evolved perturbations (m s^{-1}) based on the scaled sensitivity after 24 h of integration at 800 hPa near the crest-level height for the *U*-wind component valid at 0600 UTC 14 Jun. The GV flight track and DWSs (green dots) are shown in (a). The 700-hPa geopotential height analysis is shown in (a) with an interval of 30 m. The sensitivities in (a) are scaled by 10^5 km^{-3}.

component. The sensitive regions most strongly influence MW launching and amplitudes over South Island 24 h later. Green dots along the flight track show the DWS deployments for this assessment. The evolved perturbations (24 h) based on the sensitivity scaled to a maximum of 1 m s^{-1} at the initial time (Fig. 8b) exhibit a maximum over South Island with growth of ~10 times for the *u*-wind component perturbations in this case. The GV flight the following day on 14 June served as the verification flight to assess the degree to which the targeted DWSs improve the prediction of MWs over South Island.

MW responses in the stratosphere and MLT accompanying weak surface forcing. A major surprise during the DEEPWAVE field program was the observation of large-amplitude, breaking MWs in the MLT on a night that the flight planning team had elected not to fly a MW mission because of the forecast of weak MW forcing conditions. This quickly sensitized the team to conditions for which weak surface forcing can nevertheless lead to large MW amplitudes at high altitudes potentially because of the largely linear MW propagation and an absence of instabilities and breaking in the stratosphere, in contrast to strong forcing events (e.g., Fig. 7).

One example of these MW dynamics was observed during RF22 (13 July), a case having weak cross-mountain flow and MW forcing but favorable vertical propagation conditions with strong eastward winds through the stratosphere and above. A subset of observations from the GV lidars and the AMTM and wing cameras is shown in Figs. 9 and 10. Figures 9c and 9d show two successive cross sections along Mt. Cook flight-track 1 (MC1; see Fig. 1) of stratospheric temperatures from 20 to 60 km and sodium density perturbations obtained with the GV lidars. Figures 9a and 9b show corresponding cross sections of sodium mixing ratios for the same two cross sections. Rayleigh lidar temperatures are shown together with perturbation temperature contours from the ECMWF IFS that contributed significantly to DEEPWAVE flight planning and were interpolated to the GV location in space and time for this comparison. Note, in particular, the very close agreement of the MW scales and phase structures between the GV lidar data and a composite of IFS

analyses and 1-h predictions, including the MW growth with altitude and the changing MW vertical wavelength λ_z accompanying the stronger winds extending to ~60 km and above. The major differences are that the IFS results underpredict (by ~2–5 times) the large-scale MW amplitudes, and they appear not to capture some of the smaller-scale MWs contributing to the lidar temperature perturbations above ~40 km.

At higher altitudes, sodium mixing ratios measured by the GV sodium lidar reveal very large vertical displacements because of the smaller-scale MWs and other GWs. Peak-to-peak displacements as large as ~3–8 km imply these smaller-scale GWs have T' ~ 5–20 K or more and very large momentum fluxes. Rough estimates based on the observed GW scales and amplitudes measured on RF22 are ~100–500 $m^2 s^{-2}$ or larger, which are ~1–2 decades larger than the expected mean values at these altitudes (e.g., Fritts and Alexander 2003; Fritts et al. 2014).

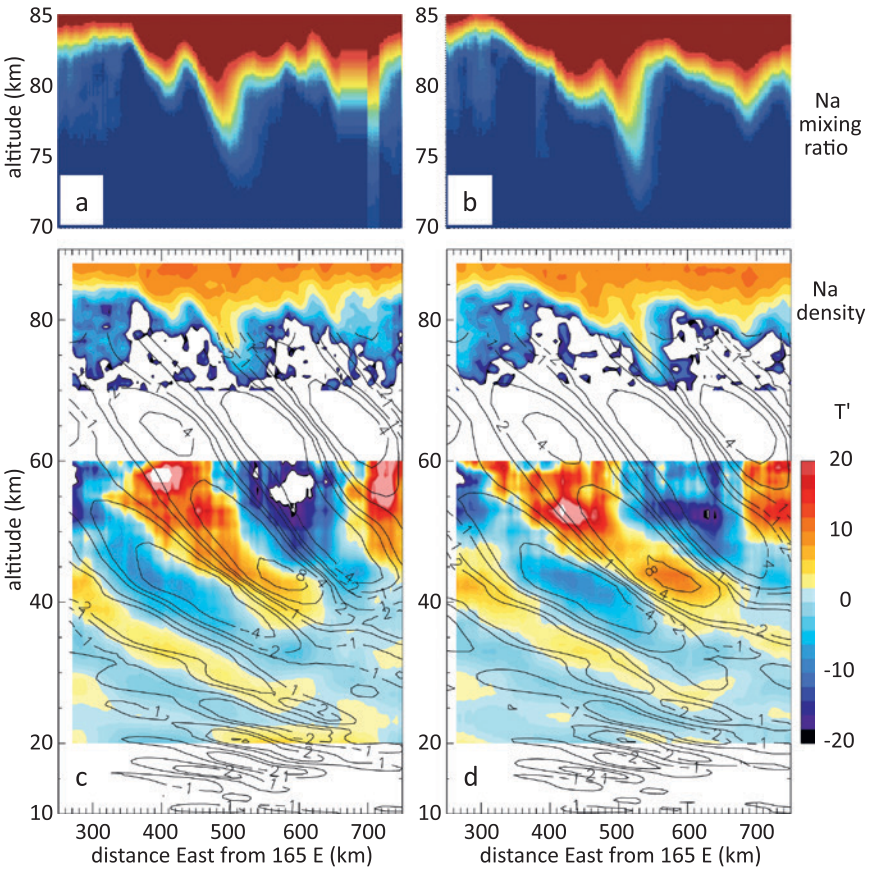

Fig. 9. GV lidar along-track vertical cross sections for the final two South Island flight segments of RF22 along MC1 (see Fig. 1) on 13 Jul. Seen are large-scale, λ_h ~ 200–300 km, MWs in the stratosphere and other smaller-scale, λ_h ~ 30–80 km, MWs and GWs in the upper stratosphere and MLT accompanying weak orographic forcing. (c),(d) Rayleigh lidar *T*' from 20 to 60 km and sodium lidar densities from 70 to 88 km. (a),(b) Sodium mixing ratios that clearly reveal vertical air parcel displacements. The Rayleigh lidar *T*' fields are shown with *T*' contours predicted by the ECMWF IFS and interpolated to the GV locations and measurement times.

An example of a combined GV AMTM and wing camera cross-mountain image of OH airglow brightness is shown in Fig. 10a for the vertical cross section shown in Fig. 9d. This reveals the same λ_h ~ 200–300-km MW seen by the Rayleigh lidar and multiple additional MWs and other GWs at smaller horizontal wavelengths, λ_h ~ 30–80 km, at ~87 km. Additional horizontal cross sections of the IFS horizontal divergence at 2 hPa (~43 km) at 0900 UT (Fig. 10b), and AIRS brightness temperature (radiance) perturbations at 2 hPa (Figs. 10c and 10d) suggest that the GV imagers observed the upward extension of the larger- and smaller-scale MW field seen by the GV lidars. The IFS vertical and horizontal cross sections in Figs. 9 and 10 captured both the vertical and horizontal structures of the large-scale MW and the associated trailing waves (TWs) for this event quite well.

Jet stream GW responses. Jet streams also represented a significant source of larger-scale GWs predicted by the NWP models during DEEPWAVE. Thus, several flights over the Southern Ocean (SO) specifically targeted these GWs. An example of one cross section through an apparent jet-generated GW, and its prediction by the IFS model, is shown in Fig. 11. As seen in the MW observations on RF22 (Fig. 9), Rayleigh lidar temperature measurements again reveal surprising agreement in the GW spatial structures and refraction with altitude with the changing environment. But again, GW amplitudes tended to be underestimated by the model fields interpolated to the GV locations and measurement times by up to ~2 times or more. While our initial comparisons employed only the IFS model, we note that other global and regional models supporting DEEPWAVE achieved similar successes in

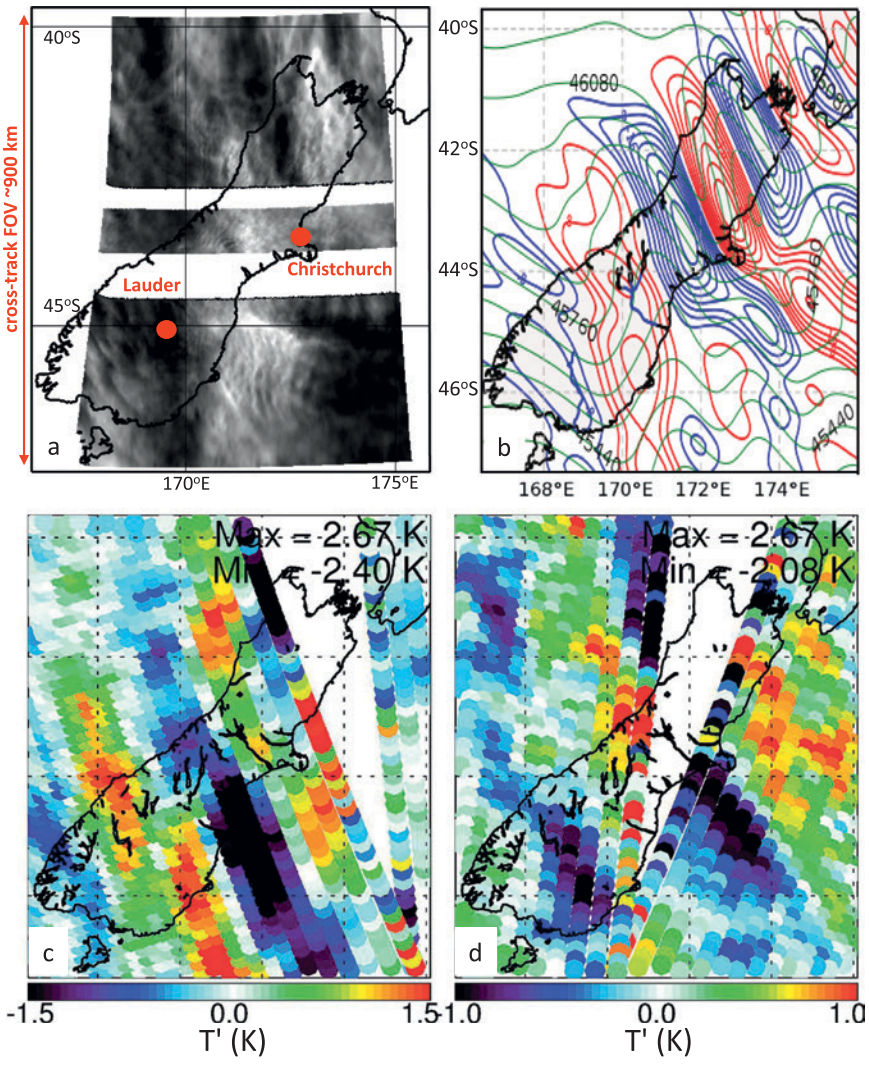

Fig. 10. (a) Full GV AMTM and wing camera flight segment image of airglow brightness at ~87 km for the final east–west flight segment over Mt. Cook obtained between 0833 and 0911 UT 13 Jul during RF22 along MC1 (see Fig. 1). Note the large-scale (λ_h ~ 200–300 km) MW having phases aligned slightly north-northwest–south-southeast and the smaller-scale GWs that are most evident in the brighter regions of the large-scale MW. ECMWF IFS horizontal divergence at 2 hPa (~43 km) at (b) 0900 UT (red positive, blue negative) and AIRS brightness temperature (radiance) perturbations (K) in swath nadir geometry from AIRS channel 74 at 2 hPa on 13 Jul during the (c) ascending and (d) descending *Aqua* overpasses of South Island. At these times, South Island lies between the outer scan edges of the AIRS swath imagery from successive satellite overpasses, separated by ~98 min and occurring at ~0141 and ~0319 UT (ascending) and ~1248 and 1427 UT (descending).

characterizing GW responses to the various sources for which the GW spatial scales were well resolved. These comparisons will be highlighted in future papers.

MW responses over small islands. Given the potentially strong MW responses at higher altitudes to flow over small SO island orography (e.g., Alexander and Grimsdell 2013), several DEEPWAVE flights overflew SO islands when deep MW forcing was expected. An example of these measurements over and in the lee of Auckland Island by the GV imagers on RF23 with strong surface flow from the northwest is shown in Fig. 12a. This image reveals ship wave temperature structure at ~87 km having a dominant λ_h ~ 40 km and evidence of a stronger trailing wave response to the north, likely resulting from filtering by the intervening winds. The GV AMTM also revealed a peak amplitude of T' ~ 20 K or larger immediately in the lee of Auckland Island. A MW response computed with the NRL Fourier–Ray (FR) linear model (Eckermann et al. 2006a) using upstream forcing profiles from NWP models and GV DWSs for this day captures some key features of the observed MLT MW field (wavelength and approximate amplitude) in Fig. 12b. Three GV passes over Auckland Island ~3–4 h later revealed breaking and instabilities that destroyed the MW field at ~87 km. As for RF22 (Fig. 9), the large amplitude and small λ_h of this response also imply a very large, but spatially localized, MW momentum flux.

MW breaking observed on 21 June. Finally, we illustrate ground-based MW observations that alerted the team to the importance of weak forcing events at high altitudes. This event occurred near the end of an interval of sustained weak MW forcing first observed on RF7 on 19 June to the southeast of South Island (e.g., AIRS images show continuous large-scale MW and trailing wave responses in the middle stratosphere throughout this interval).

Three images of OH (~87 km) temperatures obtained with the AMTM at Lauder at 30-min intervals are shown in Figs. 13a–c. These reveal relatively stationary MWs exhibiting λ_h ~ 10–70 km, phases oriented largely north (N)–south (S), and maximum $T' > 20$ K. The images also exhibit pronounced "sawtooth" patterns in the temperature fields seen as gradual decreases in temperature from warm to cold followed by sudden transitions back to warm in progressing from east to west that are indicative of GW nonlinearity, including steepening, overturning, and breaking. The Lauder AMTM images cover only a portion of the larger-scale MW response also seen simultaneously by the Lauder ASI (Fig. 13d) and by AIRS ~2 h later (Fig. 13e), both of which indicate that these MWs extend well upstream and downstream of the orographic source. They also appear for only ~1 h on this day, suggesting that filtering by variable winds at these or lower altitudes must modulate these MLT responses, given that the AIRS responses are essentially continuous throughout ~4 days. As noted for the MWs seen on RF22 and RF23 discussed above, these strong breaking MWs over Lauder must likewise have very large momentum fluxes extending in this case over a large area.

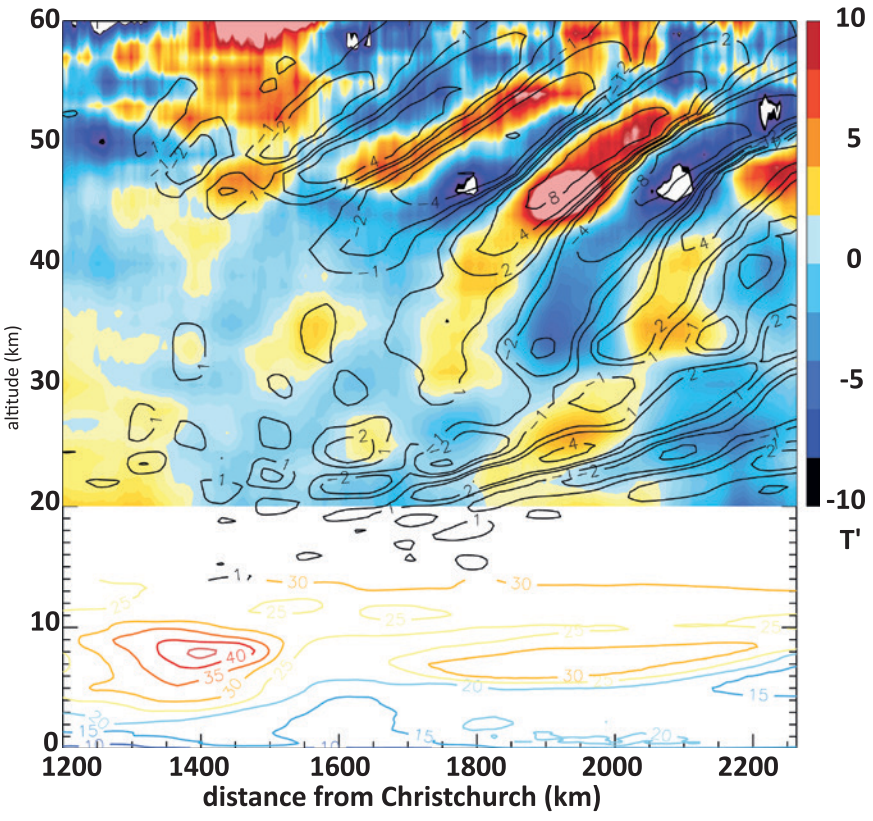

Fig. 11. As in Figs. 9c and 9d, except showing apparent stratospheric GW responses to a jet stream observed on RF25 on 18 Jul. ECMWF horizontal winds (m s^{-1}) are shown with colored contours below 15 km.

SUMMARY. The DEEPWAVE field program was successfully executed because of the major efforts by many people and organizations (see appendix D) and an unprecedented and comprehensive suite of airborne and ground-based instrumentation (see Figs. 1 and 2; Table 2). DEEPWAVE was also the first research program to systematically measure GW dynamics arising from various sources in the troposphere and stratosphere to altitudes of dissipation extending up to ~100 km. DEEPWAVE measured GWs generated by orography, jet streams, frontal systems, deep convection, and secondary generation processes and spanned a range of forcing, propagation, and dissipation conditions. The various DEEPWAVE measurements led to the initial identification of a large number of anticipated research targets (see Tables 4 and 5) and also yielded a number of surprises. These include the following:

1) highly variable MW energy fluxes at flight altitudes for weak and strong forcing;
2) the interruption of vertical MW propagation and resulting absence or strong attenuation of MWs at higher altitudes in cases of strong forcing and breaking in the stratosphere;
3) the detection of secondary GW generation in regions of strong MW breaking;
4) the potential for MWs due to weak forcing to penetrate to very high altitudes and achieve very large amplitudes and momentum fluxes;
5) the penetration of MWs having very small horizontal wavelengths of λ_h ~ 10–30-km to ~80–100-km altitudes under weak forcing conditions;
6) the generation of ship wave patterns due to small islands at small scales and large amplitudes in the MLT;
7) the ubiquitous presence of larger-scale GWs from nonorographic sources in the stratosphere and mesosphere;

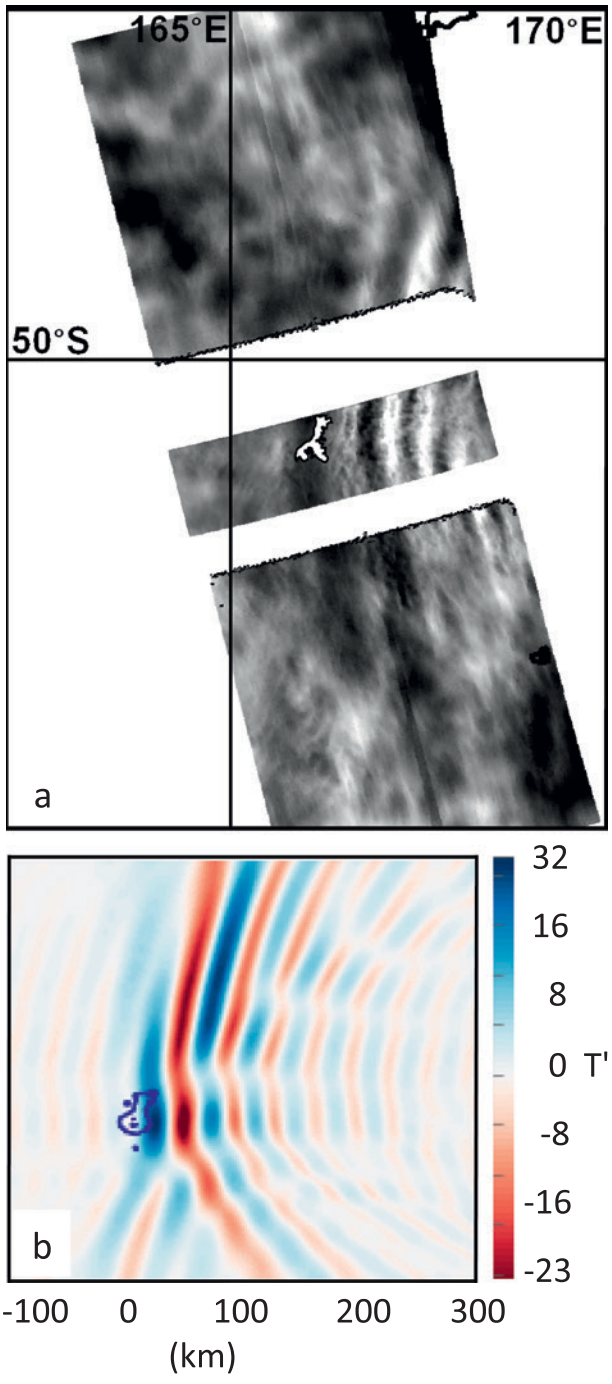

Fig. 12. As in Fig. 10a, but for (a) the first flight segment across Auckland Island on RF23. Note the strong MW and trailing wave responses in the lee and largely north of the orography. The dominant response occurs at λ_h ~ 40 km and the peak amplitude is T' > 20 K. (b) An example of the FR model prediction of this MW response at 85.5 km in an environment provided by the Navy Global Environmental Model (NAVGEM), which agrees reasonably with the observed MW phase structure and amplitude.

8) strong and coherent responses to orography and other GW sources at larger scales that were often remarkably consistent with the predictions of mesoscale and global models employed in DEEPWAVE forecasting and analysis efforts; and
9) regions of initial condition sensitivity diagnosed from adjoint models were nearly always in areas of very active weather including jet streaks, fronts, and convection that played a prominent role in GW launching the following day.

Initial conclusions from our DEEPWAVE measurements include confirmation of 1) the important roles of multiple sources of larger-scale large-amplitude GWs (λ_h ~ 200–300 km or larger) that readily penetrate to higher altitudes; 2) the frequent refraction of larger-scale GWs into the polar vortex, including large-scale trailing MWs; 3) the importance of environmental wind and temperature fields in defining their evolving characteristics and the altitudes to which they penetrate; and 4) links between GW sources and characteristics at higher altitudes. Initial DEEPWAVE observations and analyses also suggest that smaller-scale GWs 1) arise preferentially from orography, deep convection, and secondary GW generation in the stratosphere; 2) readily penetrate into the stratosphere and mesosphere under suitable propagation conditions; 3) are less likely to exhibit strong refraction into the polar vortex; 4) often attain very large amplitudes at higher altitudes; and 5) typically dominate the total momentum fluxes in these regions.

DEEPWAVE measurements also have implications for modeling of GWs arising from various sources. The high-resolution mesoscale and global models that supported DEEPWAVE appear to capture important aspects of MW generation and propagation when the MW scales are well resolved. The global models also perform well in defining the character of GW responses to various sources for larger-scale GWs. Compared to FL and lidar stratospheric measurements, however, these models typically underestimated the measured GW amplitudes in the stratosphere and above.

Specific questions suggested by initial DEEPWAVE observations and modeling that further studies will attempt to resolve include the following:

1) How do environmental conditions modulate the deep propagation of GWs from various sources?
2) What roles do nonlinear dynamics and instabilities play in interrupting GW penetration to higher altitudes?

3) Which GW sources and spatial scales contribute most to total momentum fluxes as a function of altitude, and can these be quantified by current models and satellite measurements?
4) Which GW sources and spatial scales account for the largest latitudinal transport of momentum?
5) What dynamics account for the spatial and temporal intermittency of energy and momentum fluxes at different altitudes?
6) What are the dynamics and consequences of multiscale GW superpositions throughout the lower and middle atmosphere?

Our DEEPWAVE research team is actively pursuing multiple research topics and we anticipate that a number of results will be available to the community in the near future.

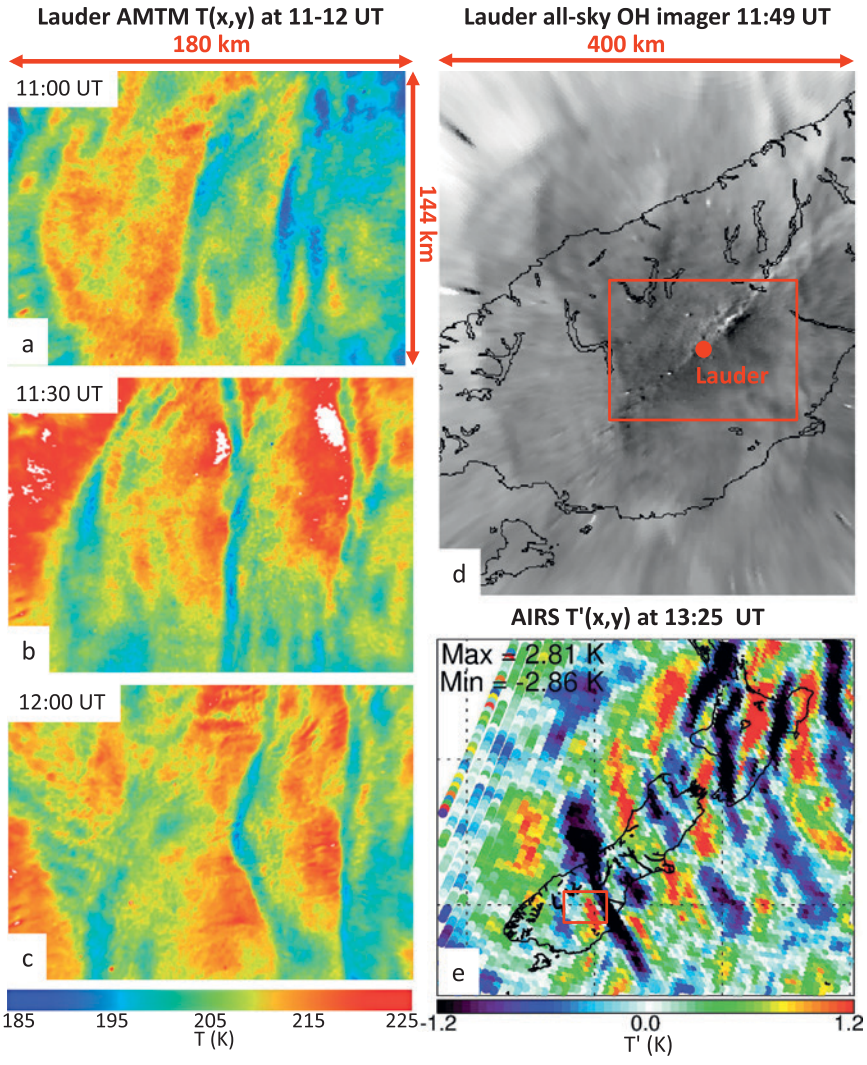

Fig. 13. Lauder AMTM images (180 km × 144 km) of MW breaking at ~82 km at (a) 1100, (b) 1130, and (c) 1200 UT 21 Jun under weak orographic forcing conditions (see the first radiosonde profile in Fig. 5). The AMTM images reveal MW responses at λ_h ~ 10–70 km that vary on time scales of ~5–10 min. The larger-scale MWs achieve temperature amplitudes of T' ~ 20 K or larger; the smaller-scale MWs exhibit amplitudes of T' ~ 5–10 K. (d) A coincident OH brightness image from the Boston University ASI at Lauder at ~82 km from the Lauder airglow imager that reveals that the AMTM images (dashed red rectangle with Lauder at the center) show only a portion of a large-scale MW response extending over a region larger than the southern South Island. (e) AIRS brightness temperature (radiance) perturbations in swath nadir imagery from channel 74 at ~2 hPa or 43 km at 1325 UT on descending *Aqua* overpass of South Island (red rectangle shows AMTM image location). Lauder AMTM and AIRS images show very similar large-scale MW responses and suggest coherent propagation of these MWs from the surface into the MLT.

ACKNOWLEDGMENTS.
The DEEPWAVE program was made possible through financial and/or in-kind support from many U.S. and international organizations, including NSF, NCAR/EOL, NRL, DLR, NIWA, AAD, the New Zealand MET Service, PAE Ltd., ECMWF, and NOAA–NCEP. Many individuals also contributed greatly in various ways (see appendix D). Financial support for U.S. participants was provided by NSF under Grants AGS-1261619 and AGS-1338646 (GATS); AGS-1338655 (Yale University); AGS-1061892 and AGS-1338666 (Utah State University); AGS-1338309 and AGS-1343097 (Boston University); and AGS-1338557 (CPI). The NRL investigators (Doyle, Eckermann, Reinecke, and Reynolds) are supported by the Chief of Naval Research through the NRL Base Program (PE 0601153N). We are indebted to Kerry Chuck and Phil Ambler for their very able assistance with airport logistics in Christchurch and to John Robinson and his very helpful NIWA staff at Lauder.

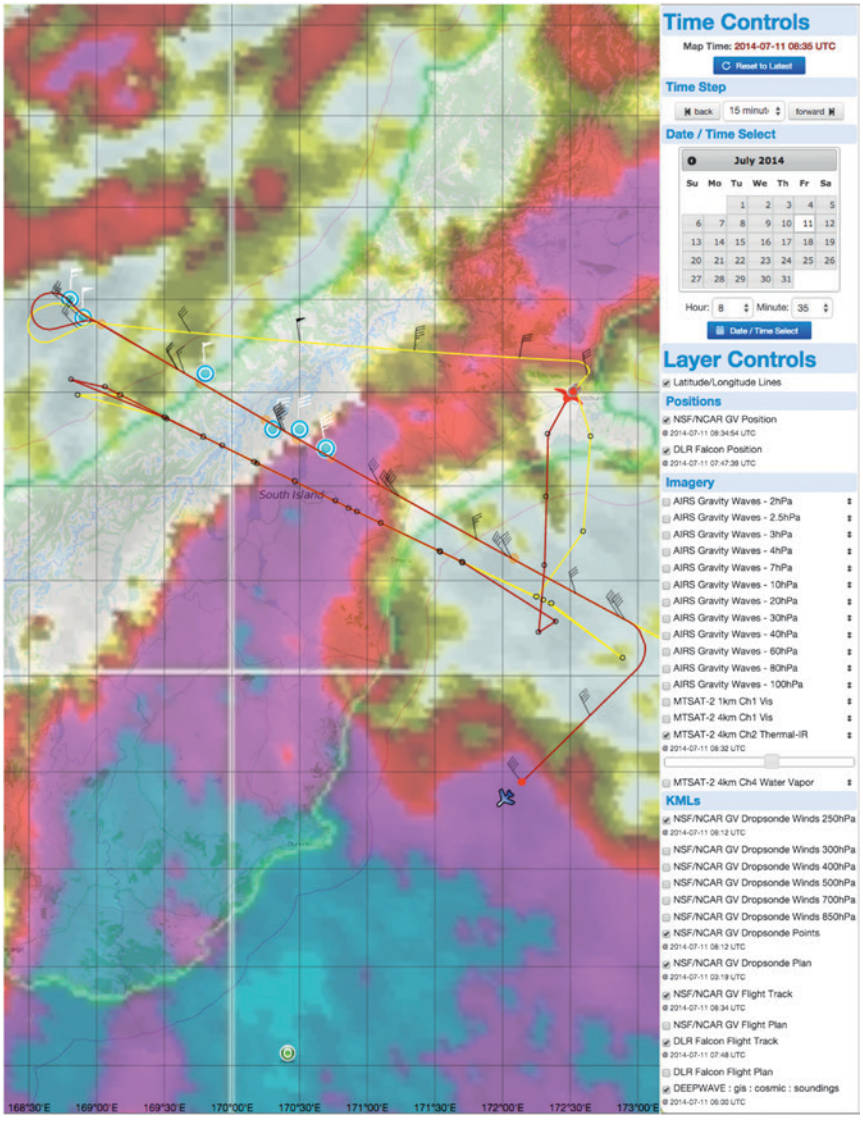

Fig. A1. Catalog maps tool display of NSF/NCAR GV and DLR Falcon flight information during flights on Jul 11. The background is from the *Multifunctional Transport Satellite-2* (*MTSAT-2*) satellite channel 2 IR image. Flight tracks for each aircraft are overlaid with aircraft icons indicating their current positions as of 0835 UTC. Wind barbs (black) are depicted at 10-min intervals along the GV flight track indicating measured flight-level winds. The blue and white circles indicate the position of DWS launch points and the white wind barbs indicate DWS winds at 250 hPa. The green and white circle south of Dunedin indicates a Constellation Observing System for Meteorology, Ionosphere and Climate (COSMIC) radio occultation sounding point. Skew *T* plots for DWSs and COSMIC data are viewable by clicking on the location circles.

APPENDIX A: DATA MANAGEMENT, FIELD CATALOG, AND ACCESS. Development and maintenance of a comprehensive data archive is a critical step in meeting the scientific objectives of DEEPWAVE. The goal is to make the dataset and documentation available to the scientific community as soon as possible following the DEEPWAVE field program via a permanent DEEPWAVE web page. This web page is available online (at www.eol.ucar.edu/field_projects/deepwave). The web page includes information on operations, logistics, facilities, instrumentation, mailing lists, meetings and presentations, education and outreach, and data management throughout the DEEPWAVE program.

EOL will maintain a DEEPWAVE data management portal that provides a long-term archive and access to DEEPWAVE datasets for the DEEPWAVE PIs and the scientific community (http://data.eol.ucar.edu/master_list/?project=DEEPWAVE), including the main archive at EOL and DEEPWAVE archives at other organizations. EOL will also ensure that "orphan" datasets (i.e., smaller regional and local networks) will remain available through the EOL DEEPWAVE archive. DEEPWAVE data will be available to the scientific community through a number of designated DEEPWAVE Data Archive Centers (DDACs), coordinated by NCAR/EOL and the main archive website noted above.

General users will have free and open access to all DEEPWAVE data, subject to procedures at the various DDACs and the terms of the DEEPWAVE data policy. Key elements of this policy include the following: 1) timely submission of preliminary and final data to an archive; 2) exclusive access to the DEEPWAVE datasets by DEEPWAVE science team members from 29 January 2015 to 29 January 2016; 3) full public data access on 1 February 2016; 4) prompt notification of data providers and offers of coauthorship or attribution by data users; and 5) proper dataset citation using digital object identifiers (DOIs) and acknowledgment of DEEPWAVE data including the project name, data providers, and funding agencies.

Table C1. DEEPWAVE participants and their roles. GATS = Global Atmospheric Technologies and Sciences. USU = Utah State University. ASPEN = Atmospheric Sounding Processing Environment. AVAPS = Airborne Vertical Atmospheric Profiling System.

Organization	Participants	DEEPWAVE roles
GATS Inc.	Dave Fritts	Lead PI, NSF/NCAR GV
	Bifford Williams	GV lidar PI and operator
	Katrina Bossert	Grad student, GV lidar operator
	Tyler Mixa	Grad student, Integrated Sounding System (ISS)/FC
	Ruth Lieberman	PW analyses
	Brian Laughman	GW modeling
Yale University	Ron Smith	Co-PI, NSF/NCAR GV
	Alison Nugent, Chris Kruse, and Campbell Watson	Grad student, FC
	Azusa Takeishi	Grad student, ISS support
	Christine Tsai	Undergrad student
USU	Mike Taylor	Co-PI, GV, PI AMTM
	Dominique Pautet	Instrument scientist, AMTM
	Neal Criddle	Grad student, Lauder AMTM
	Yucheng Zhao	Scientist, GW analyses
NRL, Monterey	Jim Doyle	Co-PI, FC/modeling
	Carolyn Reynolds	Scientist, FC/modeling
	Alex Reinecke	Scientist, FC/modeling
NRL, Washington D.C.	Steve Eckermann	Co-PI, modeling
DLR, Germany	Markus Rapp	DLR PI, Falcon and GB
	Andreas Dörnbrack	DLR co-PI, Falcon and GB
NIWA, New Zealand	Michael Uddstrom	NIWA co-PI, FC
NCAR/EOL	Jim Moore and Vidal Salazar	NCAR operations director
	Lou Lussier and Pavel Romashkin	GV project manager
	Scotty McClain, Bo LeMay, Lee Baker, and Ed Ringleman	GV pilot
	Stuart Beaton, Al Cooper, and Jorgen Jensen	GV instrument scientist/ QC
	Kip Eagan, Kyle Holden, Bill Irwin, Brent Kidd, Jason Morris, and Aaron Steinbach	GV aircraft mechanic
	John Cowan and John Munnerlyn	GV aircraft technician
	Julie Haggerty	GV MTP scientist
	Kelly Schick	GV MTP specialist
	Chris Webster	GV software engineer
	Kate Young	GV ASPEN specialist
	Clayton Arendt, Terry Hock, Nick Potts, and Laura Tudor	GV AVAPS engineer/technician
	Bill Brown	ISS project manager
	John Militizer, John Sobtzak, and Charlie Martin	ISS engineer

Table C1. Continued.

Organization	Participants	DEEPWAVE roles
NCAR/EOL	Timothy Lim, Jennifer Stanbridge, and Lou Verstraete	ISS technician
	Gary Granger	ISS support
	Chrissy Fladung	RAF administrator
	Greg Stossmeister	Field catalog manager
	Janine Aquino and Erik Johnson	Field catalog support
	Mike Paxton, Ted Russ, and Brandon Slaten	System administrator
	Steve Williams	Data management
	Alison Rockwell	EPO specialist
DLR, Germany	Andrea Hausold	DLR Falcon project manager
	Florian Gebhardt, Andreas Giez, Michael Grossrubatcher, Nico Hannemann, Christian Mallaun, Philipp Weber, Roland Welser, Alexander Wolf, and David Woudsma	DLR Falcon operations
DLR, University of Mainz (*)	Fernando Chouza-Keil, Sonja Gisinger, Peter Hoor (*), Stefan Kaufmann, Mareike Kenntner, Teresa Klausner, Michael Lichtenstern, Stefan Müller (*), Stephan Rahm, Anja Reiter, Philipp Reutter (*), Monika Scheibe, Romy Schlage, Hans Schlager, Patrick Vrancken, Christiane Voigt, and Benjamin Witschas	DLR Falcon science team
DLR	Christian Büdenbender, Bernd Kaifler, Natalie Kaifler, and Benedikt Ehard	Lauder–Rayleigh lidar
University of Innsbruck, University of Munich (Δ), DLR (*)	Martina Bramberger, Markus Garhammer (Δ), Sonja Gisinger (*), Tanja Portele, and Maria Siller	Lauder radiosonde team
NIWA	Mike Revelle and Richard Turner	Forecasting
	Tony Bromley	Haast sounding support
University of Innsbruck	Johannes Wagner	Grad student, FC/modeling
Computational Physics Inc.	Jun Ma and Dave Broutman	Scientist, FC
University of Canterbury	Joe Chen, Ben Jolly, Jordan Miller, Simon Parson, David Stevens, and Kate Walsh	Student, ISS support
Australian Antarctic Division	Damian Murphy, Andrew Klekociuk, and Peter Love	Kingston meteor radar and lidar
Boston University	Steve Smith	Lauder and MJO ASIs
University of Washington	Gonzalo Hernandez and Michael McCarthy	MJO FPI
University of Adelaide	Iain Reid, Andrew Mackinnon, and Andrew Spargo	Kingston meteor radar
St. Cloud State University	Brian Billings	Scientist, surface observations/photography
	Tashiana Osborne	Grad Student, ISS support
New Zealand Meteorological Service	Peter Kreft and Tony Qualye	
Millersville University	Mike Charnick	Grad student, FC
Australian Bureau of Meteorology	Michael Joyce, David Nottage, Greg Roff, and Keon Stevenson	Radiosondes, Hobart, Tasmania, and Macquarie Island

An online DEEPWAVE field catalog (http://catalog.eol.ucar.edu/deepwave) was hosted by EOL during the DEEPWAVE field program to support mission planning, product displays, documentation of activities, and "browse" tools for use in postfield analyses. The DEEPWAVE field catalog can access and replay flight missions and supports real-time mission coordinator and geographical information system (GIS) catalog maps display tools. The 2013 DEEPWAVE flight planning exercise is documented online (http://catalog.eol.ucar.edu/deepwave_2013). An example of the field catalog maps display is shown for reference in Fig. A1.

APPENDIX B: DEEPWAVE FIELD OPERATIONS. Operational support for the DEEPWAVE field program included several major components. The DEEPWAVE Operations Center and aircraft support were located at the U.S. Antarctic Program (USAP) Christchurch International Airport (CHC). Major logistical support was provided by PAE Ltd., the local New Zealand contractor funded by NSF. The project occupied two buildings and adjacent ramp space and served as the focus for aircraft support, forecasting and in-field science analyses, logistics, and communications. Broadband Internet access facilitated communications with remote participants in New Zealand and elsewhere.

The major deployments of ground-based instruments and aircraft for DEEPWAVE occurred over the period from late May to early August 2014, though several instruments or capabilities remained up to several months longer at Lauder. More information on these efforts and related activities can be found online (www.eol.ucar.edu/field_projects/deepwave).

The science leadership, operations coordinators, and facility project managers were key components of the DEEPWAVE in-field management team. DEEPWAVE had a daily planning meeting (DPM) 7 days a week to discuss relevant operations issues, resources and status, science objective status, current weather and outlook, and PI science mission proposals. An interesting aspect of DEEPWAVE was that all GV flights but one were conducted at night to allow the new GV optical instruments to perform optimally. The DPM was convened at 0100 UTC (1300 LT) 7 days a week to allow participation by as many groups as possible across 10 time zones. ReadyTalk web conferencing linked participants with full audio and video capabilities. The DPMs led to the definitions of the various IOPs and RF and GB measurement scheduling.

Real-time support for the project including tracking of, and interactions with, the GV utilizing the DEEPWAVE field catalog and the EOL/Research Aviation Facility (RAF) Aeros and catalog maps tools for displaying real-time aircraft position, flight-level data displays, satellite and model data overlays, dropsonde launches and plots, and lidar and AMTM data sharing.

A unique aspect of DEEPWAVE was the ability to make real-time dropsonde deployment decisions at specific points over New Zealand and widely over the Southern Ocean. These data were relayed via satellite to the ground for quality control and processing by EOL-trained student participants before forwarding to the Global Telecommunications System for assimilation into global weather center model forecasts.

APPENDIX C: DEEPWAVE PARTICIPANTS AND ROLES. Table C1 shows the DEEPWAVE participants and their roles during the experiment.

REFERENCES

Alexander, M. J., and L. Pfister, 1995: Gravity wave momentum flux in the lower stratosphere over convection. *Geophys. Res. Lett.*, **22**, 2029–2032, doi:10.1029/95GL01984.

——, and A. W. Grimsdell, 2013: Seasonal cycle of orographic gravity wave occurrence above small islands in the Southern Hemisphere: Implications for effects on the general circulation. *J. Geophys. Res. Atmos.*, **118**, 11 589–11 599, doi:10.1002/2013JD020526.

——, S. D. Eckermann, D. Broutman, and J. Ma, 2009: Momentum flux estimates for South Georgia Island mountain waves in the stratosphere observed via satellite. *Geophys. Res. Lett.*, **36**, L12816, doi:10.1029/2009GL038587.

——, and Coauthors, 2010: Recent developments in gravity-wave effects in climate models and the global distribution of gravity-wave momentum flux from observations and models. *Quart. J. Roy. Meteor. Soc.*, **136**, 1103–1124, doi:10.1002/qj.637.

Alexander, S. P., A. R. Klekociuk, and D. J. Murphy, 2011: Rayleigh lidar observations of gravity wave activity in the winter upper stratosphere and lower mesosphere above Davis, Antarctica (69°S, 78°E). *J. Geophys. Res.*, **116**, D13109, doi:10.1029/2010JD015164.

Allen, S. J., and R. A. Vincent, 1995: Gravity wave activity in the lower atmosphere: Seasonal and latitudinal variations. *J. Geophys. Res.*, **100**, 1327–1350, doi:10.1029/94JD02688.

Amerault, C., X. Zou, and J. Doyle, 2008: Tests of an adjoint mesoscale model with explicit moist physics on the cloud scale. *Mon. Wea. Rev.*, **136**, 2120–2132, doi:10.1175/2007MWR2259.1.

Atlas, D., J. I. Metcalf, J. H. Richter, and E. E. Gossard, 1970: The birth of "CAT" and microscale turbulence. *J. Atmos. Sci.*, **27**, 903–913, doi:10.1175/1520-0469(1970)027<0903:TBOAMT>2.0.CO;2.

Bacmeister, J. T., M. F. Wehner, R. B. Neale, A. Gettelman, C. Hannay, P. H. Lauritzen, J. M. Caron, and J. E. Truesdale, 2014: Exploratory high-resolution climate simulations using the Community Atmosphere Model (CAM). *J. Climate*, **27**, 3073–3099, doi:10.1175/JCLI-D-13-00387.1.

Balsley, B. B., and R. Garello, 1985: The kinetic energy density in the troposphere, stratosphere, and mesosphere: A preliminary study using the Poker Flat MST radar in Alaska. *Radio Sci.*, **20**, 1355–1361, doi:10.1029/RS020i006p01355.

Booker, J. R., and F. P. Bretherton, 1967: The critical layer for internal gravity waves in a shear flow. *J. Fluid Mech.*, **27**, 513–539, doi:10.1017/S0022112067000515.

Bougeault, P., A. Jansa Clar, B. Benech, B. Carissimo, J. Pelon, and E. Richard, 1990: Momentum budget over the Pyrénées: The PYREX experiment. *Bull. Amer. Meteor. Soc.*, **71**, 806–818, doi:10.1175/1520-0477(1990)071<0806:MBOTPT>2.0.CO;2.

——, and Coauthors, 2001: The MAP special observing period. *Bull. Amer. Meteor. Soc.*, **82**, 433–462, doi:10.1175/1520-0477(2001)082<0433:TMSOP>2.3.CO;2.

Bretherton, F. P., 1969a: Waves and turbulence in stably stratified fluids. *Radio Sci.*, **4**, 1279–1287, doi:10.1029/RS004i012p01279.

——, 1969b: Momentum transfer by gravity waves. *Quart. J. Roy. Meteor. Soc.*, **95**, 213–243, doi:10.1002/qj.49709540402.

Brinkmann, W. A. R., 1974: Strong downslope winds at Boulder, Colorado. *Mon. Wea. Rev.*, **102**, 592–602, doi:10.1175/1520-0493(1974)102<0592:SDWABC>2.0.CO;2.

Brown, P. R. A., 1983: Aircraft measurements of mountain waves and their associated momentum flux over the British Isles. *Quart. J. Roy. Meteor. Soc.*, **109**, 849–865, doi:10.1002/qj.49710946211.

Bühler, O., 2014: *Waves and Mean Flows*. Cambridge University Press, 360 pp.

Carslaw, K. S., and Coauthors, 1998: Particle microphysics and chemistry in remotely observed mountain polar stratospheric clouds. *J. Geophys. Res.*, **103**, 5785–5796, doi:10.1029/97JD03626.

Chanin, M.-L., and A. Hauchecorne, 1981: Lidar observation of gravity and tidal waves in the stratosphere and mesosphere. *J. Geophys. Res.*, **86**, 9715–9721, doi:10.1029/JC086iC10p09715.

Clark, T. L., and W. R. Peltier, 1977: On the evolution and stability of finite-amplitude mountain waves. *J. Atmos. Sci.*, **34**, 1715–1730, doi:10.1175/1520-0469(1977)034<1715:OTEASO>2.0.CO;2.

Dewan, E. M., and Coauthors, 1998: MSX satellite observations of thunderstorm-generated gravity waves in mid-wave infrared images of the upper stratosphere. *Geophys. Res. Lett.*, **25**, 939–942, doi:10.1029/98GL00640.

Dörnbrack, A., M. Leutbecher, J. Reichardt, A. Behrendt, K.-P. Müller, and G. Baumgarten, 2001: Relevance of mountain wave cooling for the formation of polar stratospheric clouds over Scandinavia: Mesoscale dynamics and observations for January 1997. *J. Geophys. Res.*, **106**, 1569–1581, doi:10.1029/2000JD900194.

Doyle, J. D., and R. B. Smith, 2003: Mountain waves over the Hohe Tauern: Influence of upstream diabatic effects. *Quart. J. Roy. Meteor. Soc.*, **129**, 799–823, doi:10.1256/qj.01.205.

——, and Q. Jiang, 2006: Observations and numerical simulations of mountain waves in the presence of directional wind shear. *Quart. J. Roy. Meteor. Soc.*, **132**, 1877–1905, doi:10.1256/qj.05.140.

——, and Coauthors, 2000: An intercomparison of model-predicted wave breaking for the 11 January 1972 Boulder windstorm. *Mon. Wea. Rev.*, **128**, 901–914, doi:10.1175/1520-0493(2000)128<0901:AIOMPW>2.0.CO;2.

——, M. Shapiro, Q. Jiang, and D. Bartels, 2005: Large-amplitude mountain wave breaking over Greenland. *J. Atmos. Sci.*, **62**, 3106–3126, doi:10.1175/JAS3528.1.

——, and Coauthors, 2011: An intercomparison of T-REX mountain-wave simulations and implications for mesoscale predictability. *Mon. Wea. Rev.*, **139**, 2811–2831, doi:10.1175/MWR-D-10-05042.1.

——, C. Amerault, C. A. Reynolds, and P. A. Reinecke, 2014: Initial condition sensitivity and predictability of a severe extratropical cyclone using a moist adjoint. *Mon. Wea. Rev.*, **142**, 320–342, doi:10.1175/MWR-D-13-00201.1.

Duck, T. J., J. A. Whiteway, and A. I. Carswell, 2001: The gravity wave–Arctic stratospheric vortex interaction. *J. Atmos. Sci.*, **58**, 3581–3596, doi:10.1175/1520-0469(2001)058<3581:TGWASV>2.0.CO;2.

Eckermann, S. D., and P. Preusse, 1999: Global measurements of stratospheric mountain waves from space. *Science*, **286**, 1534–1537, doi:10.1126/science.286.5444.1534.

——, and D. L. Wu, 2012: Satellite detection of orographic gravity-wave activity in the winter subtropical stratosphere over Australia and Africa. *Geophys. Res. Lett.*, **39**, L21807, doi:10.1029/2012GL053791.

——, D. Broutman, J. Ma, and J. Lindeman, 2006a: Fourier-ray modeling of short wavelength trapped lee waves observed in infrared satellite imagery near Jan

Mayen. *Mon. Wea. Rev.*, **134**, 2830–2848, doi:10.1175/MWR3218.1.

——, A. Dörnbrack, S. B. Vosper, H. Flentje, M. J. Mahoney, T. P. Bui, and K. S. Carslaw, 2006b: Mountain wave–induced polar stratospheric cloud forecasts for aircraft science flights during SOLVE/THESEO 2000. *Wea. Forecasting*, **21**, 42–68, doi:10.1175/WAF901.1.

——, J. Ma, and D. L. Wu, 2007: A three-dimensional mountain wave imaged in satellite radiance throughout the stratosphere: Evidence of the effects of directional wind shear. *Quart. J. Roy. Meteor. Soc.*, **133**, 1959–1974, doi:10.1002/qj.187.

——, L. Hoffman, M. Hopfner, D. L. Wu, and M. J. Alexander, 2009: Antarctic NAT PSC belt of June 2003: Observational validation of the mountain wave seeding hypothesis. *Geophys. Res. Lett.*, **36**, L02807, doi:10.1029/2008GL036629.

Eliassen, A., and E. Palm, 1961: On the transfer of energy in stationary mountain waves. *Geofys. Publ.*, **22**, 1–23.

Ern, M., P. Preusse, M. J. Alexander, and C. D. Warner, 2004: Absolute values of gravity wave momentum flux derived from satellite data. *J. Geophys. Res.*, **109**, D20103, doi:10.1029/2004JD004752.

Fritts, D. C., 1984: Gravity wave saturation in the middle atmosphere: A review of theory and observations. *Rev. Geophys.*, **22**, 275–308, doi:10.1029/RG022i003p00275.

——, and P. K. Rastogi, 1985: Convective and dynamical instabilities due to gravity wave motions in the lower and middle atmosphere: Theory and observations. *Radio Sci.*, **20**, 1247–1277, doi:10.1029/RS020i006p01247.

——, and R. A. Vincent, 1987: Mesospheric momentum flux studies at Adelaide, Australia: Observations and a gravity wave/tidal interaction model. *J. Atmos. Sci.*, **44**, 605–619, doi:10.1175/1520-0469(1987)044<0605:MMFSAA>2.0.CO;2.

——, and G. D. Nastrom, 1992: Sources of mesoscale variability of gravity waves. Part II: Frontal, convective, and jet stream excitation. *J. Atmos. Sci.*, **49**, 111–127, doi:10.1175/1520-0469(1992)049<0111:SOMVOG>2.0.CO;2.

——, and M. J. Alexander, 2003: Gravity dynamics and effects in the middle atmosphere. *Rev. Geophys.*, **41**, 1003, doi:10.1029/2001RG000106.

——, S. A. Vadas, and Y. Yamada, 2002: An estimate of strong local gravity wave body forcing based on OH airglow and meteor radar observations. *Geophys. Res. Lett.*, **29**, doi:10.1029/2001GL013753.

——, L. Wang, J. Werne, T. Lund, and K. Wan, 2009: Gravity wave instability dynamics at high Reynolds numbers. Part II: Turbulence evolution, structure, and anisotropy. *J. Atmos. Sci.*, **66**, 1149–1171, doi:10.1175/2008JAS2727.1.

——, and Coauthors, 2014: Quantifying gravity wave momentum fluxes with mesosphere temperature mappers and correlative instrumentation. *J. Geophys. Res. Atmos.*, **119**, 13 583–13 603, doi:10.1002/2014JD022150.

Garcia, R. R., and S. Solomon, 1985: The effect of breaking gravity waves on the dynamical and chemical composition of the mesosphere and lower thermosphere. *J. Geophys. Res.*, **90**, 3850–3868, doi:10.1029/JD090iD02p03850.

Gardner, C. S., and D. G. Voelz, 1987: Lidar studies of the nighttime sodium layer over Urbana, Illinois: 2. Gravity waves. *J. Geophys. Res.*, **92**, 4673–4694, doi:10.1029/JA092iA05p04673.

Gavrilov, N. M., and G. M. Shved, 1982: Study of internal gravity waves in the lower thermosphere from observations of the nocturnal sky airglow [OI] 5577 A in Ashkhabad (translation). *Ann. Geophys.*, **38**, 789–803.

Geller, M. A., and Coauthors, 2013: A comparison between gravity wave momentum fluxes in observations and climate models. *J. Climate*, **26**, 6383–6405, doi:10.1175/JCLI-D-12-00545.1.

Goldberg, R. A., and Coauthors, 2006: The MaCWAVE program to study gravity wave influences on the polar mesosphere. *Ann. Geophys.*, **24**, 1159–1173, doi:10.5194/angeo-24-1159-2006.

Gong, J., D. L. Wu, and S. D. Eckermann, 2012: Gravity wave variances and propagation derived from AIRS radiances. *Atmos. Chem. Phys.*, **12**, 1701–1720, doi:10.5194/acp-12-1701-2012.

Gossard, E. E., and W. H. Hooke, 1975: *Waves in the Atmosphere.* Developments in Atmospheric Science Series, Vol. 2, Elsevier Scientific, 456 pp.

——, J. H. Richter, and D. Atlas, 1970: Internal waves in the atmosphere from high-resolution radar measurements. *J. Geophys. Res.*, **75**, 3523–3536, doi:10.1029/JC075i018p03523.

Grubišić, V., and J. M. Lewis, 2004: Sierra Wave Project revisited: 50 years later. *Bull. Amer. Meteor. Soc.*, **85**, 1127–1142, doi:10.1175/BAMS-85-8-1127.

——, and Coauthors, 2008: The Terrain-Induced Rotor Experiment. *Bull. Amer. Meteor. Soc.*, **89**, 1513–1533, doi:10.1175/2008BAMS2487.1.

Haynes, P. H., C. J. Marks, M. E. McIntyre, T. G. Shephard, and K. P. Shine, 1991: On the "downward control" of extratropical diabatic circulations by eddy-induced mean zonal forces. *J. Atmos. Sci.*, **48**, 651–678, doi:10.1175/1520-0469(1991)048<0651:OTCOED>2.0.CO;2.

Hecht, J. H., R. L. Walterscheid, D. C. Fritts, J. R. Isler, D. C. Senft, C. S. Gardner, and S. J. Franke, 1997: Wave breaking signatures in OH airglow and sodium densities and temperatures: 1. Airglow imaging, Na lidar, and MF radar observations. *J. Geophys. Res.*, **102**, 6655–6668, doi:10.1029/96JD02619.

——, ——, and R. Vincent, 2001: Airglow observations of dynamical (wind shear-induced) instabilities over Adelaide, Australia, associated with atmospheric gravity waves. *J. Geophys. Res.*, **106**, 28 189–28 197, doi:10.1029/2001JD000419.

——, and Coauthors, 2014: The life cycle of instability features measured from the Andes Lidar Observatory over Cerro Pachon on March 24, 2012. *J. Geophys. Res. Atmos.*, **119**, 8872–8898, doi:10.1002/2014JD021726.

Hendricks, E. A., J. D. Doyle, S. D. Eckermann, Q. Jiang, and P. A. Reinecke, 2014: What is the source of the stratospheric gravity wave belt in austral winter? *J. Atmos. Sci.*, **71**, 1583–1592, doi:10.1175/JAS-D-13-0332.1.

Hertzog, A., G. Boccara, R. A. Vincent, F. Vial, and P. Cocquerez, 2008: Estimation of gravity-wave momentum fluxes and phase speeds from quasi-Lagrangian stratospheric balloon flights. Part II: Results from the Vorcore campaign in Antarctica. *J. Atmos. Sci.*, **65**, 3056–3070, doi:10.1175/2008JAS2710.1.

——, M. J. Alexander, and R. Plougonven, 2012: On the intermittency of gravity wave momentum flux in the stratosphere. *J. Atmos. Sci.*, **69**, 3433–3448, doi:10.1175/JAS-D-12-09.1.

Hines, C. O., 1960: Internal atmospheric gravity waves at ionospheric heights. *Can. J. Phys.*, **38**, 1441–1481, doi:10.1139/p60-150.

——, 1991: The saturation of gravity waves in the middle atmosphere. Part II: Development of Doppler-spread theory. *J. Atmos. Sci.*, **48**, 1361–1379, doi:10.1175/1520-0469(1991)048<1361:TSOGWI>2.0.CO;2.

——, 1997a: Doppler-spread parameterization of gravity-wave momentum deposition in the middle atmosphere. Part 1: Basic formulation. *J. Atmos. Sol.-Terr. Phys.*, **59**, 371–386, doi:10.1016/S1364-6826(96)00079-X.

——, 1997b: Doppler-spread parameterization of gravity-wave momentum deposition in the middle atmosphere. Part 2: Broad and quasi-monochromatic spectra, and implementation. *J. Atmos. Sol.-Terr. Phys.*, **59**, 387–400, doi:10.1016/S1364-6826(96)00080-6.

Holton, J. R., 1982: The role of gravity wave induced drag and diffusion in the momentum budget of the mesosphere. *J. Atmos. Sci.*, **39**, 791–799, doi:10.1175/1520-0469(1982)039<0791:TROGWI>2.0.CO;2.

Hostetler, C. A., and C. S. Gardner, 1994: Observations of horizontal and vertical wave number spectra of gravity wave motions in the stratosphere and mesosphere over the mid-Pacific. *J. Geophys. Res.*, **99**, 1283–1302, doi:10.1029/93JD02927.

——, ——, R. A. Vincent, and D. Lesicar, 1991: Spectra of gravity wave density and wind perturbations observed during ALOHA-90 on the 25 March flight between Maui and Christmas Island. *Geophys. Res. Lett.*, **18**, 1325–1328, doi:10.1029/91GL01150.

Kim, Y.-J., S. D. Eckermann, and H.-Y. Chun, 2003: An overview of the past, present and future of gravity-wave drag parameterization for numerical climate and weather prediction models. *Atmos.–Ocean*, **41**, 65–98, doi:10.3137/ao.410105.

Klemp, J. B., and D. K. Lilly, 1978: Numerical simulation of hydrostatic mountain waves. *J. Atmos. Sci.*, **35**, 78–107, doi:10.1175/1520-0469(1978)035<0078:NSOHMW>2.0.CO;2.

Kruse, C. G. and R. B. Smith, 2015: Gravity wave diagnostics and characteristics in mesoscale fields. *J. Atmos. Sci.*, **72**, 4372–4392, doi:10.1175/JAS-D-15-0079.1.

Kuettner, J. P., and D. K. Lilly, 1968: Lee waves in the Colorado Rockies. *Weatherwise*, **21**, 180–197, doi:10.1080/00431672.1968.9932819.

——, P. A. Hildebrand, and T. L. Clark, 1987: Convection waves: Observations of gravity wave systems over convectively active boundary layers. *Quart. J. Roy. Meteor. Soc.*, **113**, 445–467, doi:10.1002/qj.49711347603.

Küttner, J., 1938: Moazagotl und Föhnwelle. *Beitr. Phys. Atmos.*, **25**, 79–114.

——, 1939: Zur Entstehung der Föhnwelle. *Beitr. Phys. Atmos.*, **25**, 251–299.

Lilly, D. K., 1978: A severe downslope windstorm and aircraft turbulence induced by a mountain wave. *J. Atmos. Sci.*, **35**, 59–77, doi:10.1175/1520-0469(1978)035<0059:ASDWAA>2.0.CO;2.

——, and P. J. Kennedy, 1973: Observations of a stationary mountain wave and its associated momentum flux and energy dissipation. *J. Atmos. Sci.*, **30**, 1135–1152, doi:10.1175/1520-0469(1973)030<1135:OOASMW>2.0.CO;2.

——, J. M. Nicholls, P. J. Kennedy, J. B. Klemp, and R. M. Chervin, 1982: Aircraft measurements of wave momentum flux over the Colorado Rocky Mountains. *Quart. J. Roy. Meteor. Soc.*, **108**, 625–642, doi:10.1002/qj.49710845709.

Lindzen, R. S., 1981: Turbulence and stress owing to gravity wave and tidal breakdown. *J. Geophys. Res.*, **86**, 9707–9714, doi:10.1029/JC086iC10p09707.

——, and J. R. Holton, 1968: A theory of the quasi-biennial oscillation. *J. Atmos. Sci.*, **25**, 1095–1107,

doi:10.1175/1520-0469(1968)025<1095:ATOTQB>2.0.CO;2.

Liu, H.-L., J. M. McInerney, S. Santos, P. H. Lauritzen, M. A. Taylor, and N. M. Pedatella, 2014: Gravity waves simulated by high-resolution Whole Atmosphere Community Climate Model. *Geophys. Res. Lett.*, **41**, 9106–9112, doi:10.1002/2014GL062468.

Lombard, P. N., and J. J. Riley, 1996: Instability and breakdown of internal gravity waves. I. Linear stability analysis. *Phys. Fluids*, **8**, 3271–3287, doi:10.1063/1.869117.

Long, R. R., 1953: Some aspects of the flow of stratified fluids. I. A theoretical investigation. *Tellus*, **5**, 42–58, doi:10.1111/j.2153-3490.1953.tb01035.x.

——, 1955: Some aspects of the flow of stratified fluids. III. Continuous density gradients. *Tellus*, **7**, 341–357, doi:10.1111/j.2153-3490.1955.tb01171.x.

Lu, X., X. Chu, W. Fong, C. Chen, Z. Yu, B. R. Roberts, and A. J. McDonald, 2015: Vertical evolution of potential energy density and vertical wave number spectrum of Antarctic gravity waves from 35 to 105 km at McMurdo (77.8°S, 166.7°E). *J. Geophys. Res. Atmos.*, **120**, 2719–2737, doi:10.1002/2014JD022751.

Luce, H., M. Yamamoto, S. Fukao, and K. Sato, 2008: High-resolution observations with MU radar of a KH instability triggered by an inertia–gravity wave in the upper part of the jet stream. *J. Atmos. Sci.*, **65**, 1711–1718, doi:10.1175/2007JAS2346.1.

Manley, G., 1945: The helm wind of Crossfell, 1937–1939. *Quart. J. Roy. Meteor. Soc.*, **71**, 197–219, doi:10.1002/qj.49707130901.

McFarlane, N. A., 1987: The effect of orographically excited gravity wave drag on the general circulation of the lower stratosphere and troposphere. *J. Atmos. Sci.*, **44**, 1775–1800, doi:10.1175/1520-0469(1987)044<1775:TEOOEG>2.0.CO;2.

Nakamura, T., T. Aono, T. Tsuda, A. G. Admiranto, E. Achmad, and Suranto, 2003: Mesospheric gravity waves over a tropical convective region observed by OH airglow imaging in Indonesia. *Geophys. Res. Lett.*, **30**, 1882, doi:10.1029/2003GL017619.

Nappo, C. J., 2013: *An Introduction to Atmospheric Gravity Waves.* 2nd ed. International Geophysics Series, Vol. 85, Academic Press, 276 pp.

Nastrom, G. D., and D. C. Fritts, 1992: Sources of mesoscale variability of gravity waves. Part I: Topographic excitation. *J. Atmos. Sci.*, **49**, 101–110, doi:10.1175/1520-0469(1992)049<0101:SOMVOG>2.0.CO;2.

Pautet, P.-D., M. J. Taylor, W. R. Pendleton Jr., Y. Zhao, T. Yuan, R. Esplin, and D. McLain, 2014: An advanced mesospheric temperature mapper for high-latitude airglow studies. *Appl. Opt.*, **53**, 5934–5943, doi:10.1364/AO.53.005934.

Pavelin, E., J. A. Whiteway, and G. Vaughants, 2001: Observation of gravity wave generation and breaking in the lowermost stratosphere. *J. Geophys. Res.*, **106**, 5173–5179, doi:10.1029/2000JD900480.

Pfister, L., S. Scott, M. Loewenstein, S. Bowen, and M. Legg, 1993: Mesoscale disturbances in the tropical stratosphere excited by convection: Observations and effects on the stratospheric momentum budget. *J. Atmos. Sci.*, **50**, 1058–1075, doi:10.1175/1520-0469(1993)050<1058:MDITTS>2.0.CO;2.

Plougonven, R., A. Hertzog, and H. Teitelbaum, 2008: Observations and simulations of a large-amplitude mountain wave breaking over the Antarctic Peninsula. *J. Geophys. Res.*, **113**, D16113, doi:10.1029/2007JD009739.

——, ——, and L. Guez, 2013: Gravity waves over Antarctica and the Southern Ocean: Consistent momentum fluxes in mesoscale simulations and stratospheric balloon observations. *Quart. J. Roy. Meteor. Soc.*, **139**, 101–118, doi:10.1002/qj.1965.

Preusse, P., S. D. Eckerman, and M. Ern, 2008: Transparency of the atmosphere to short horizontal wavelength gravity waves. *J. Geophys. Res.*, **113**, D24104, doi:10.1029/2007JD009682.

Queney, M. P., 1936a: Recherches relatives a l'influence du relief sur les éléments météorologiques (1). *Meteorologie*, 334–353.

——, 1936b: Recherches relatives a l'influence du relief sur les éléments météorologiques (suite). *Meteorologie*, 453–470.

——, 1947: Theory of perturbations in stratified currents with application to air flow over mountain barriers. Department of Meteorology, University of Chicago Miscellaneous Rep. 23, 81 pp.

Rapp, M., B. Strelnikov, A. Müllemann, F.-J. Lübken, and D. C. Fritts, 2004: Turbulence measurements and implications for gravity wave dissipation during the MaCWAVE/MIDAS summer rocket program. *Geophys. Res. Lett.*, **31**, L24S07, doi:10.1029/2003GL019325.

Sato, K., 1994: A statistical study of the structure, saturation and sources of inertio-gravity waves in the lower stratosphere observed with the MU radar. *J. Atmos. Terr. Phys.*, **56**, 755–774, doi:10.1016/0021-9169(94)90131-7.

——, and R. F. Woodman, 1982: Fine altitude resolution radar observations of stratospheric turbulent layers by the Arecibo 430 MHz radar. *J. Atmos. Sci.*, **39**, 2546–2552, doi:10.1175/1520-0469(1982)039<2546:FAROOS>2.0.CO;2.

——, and T. J. Dunkerton, 1997: Estimates of momentum flux associated with equatorial Kelvin and gravity waves. *J. Geophys. Res.*, **102**, 26 247–26 261, doi:10.1029/96JD02514.

——, and M. Yoshiki, 2008: Gravity wave generation around the polar vortex in the stratosphere revealed by 3-hourly radiosonde observations at Syowa station. *J. Atmos. Sci.*, **65**, 3719–3735, doi:10.1175/2008JAS2539.1.

——, S. Tateno, S. Watanabe, and Y. Kawatani, 2012: Gravity wave characteristics in the Southern Hemisphere revealed by a high-resolution middle-atmosphere general circulation model. *J. Atmos. Sci.*, **69**, 1378–1396, doi:10.1175/JAS-D-11-0101.1.

Scorer, R. S., 1949: Theory of waves in the lee of mountains. *Quart. J. Roy. Meteor. Soc.*, **75**, 41–46, doi:10.1002/qj.49707532308.

She, C. Y., J. R. Yu, J. W. Huang, C. Nagasawa, and C. S. Gardner, 1991: Na temperature lidar measurements of gravity wave perturbations of wind, density and temperature in the mesopause region. *Geophys. Res. Lett.*, **18**, 1329–1331, doi:10.1029/91GL01517.

Shutts, G. J., and S. B. Vosper, 2011: Stratospheric gravity waves revealed in NWP model forecasts. *Quart. J. Roy. Meteor. Soc.*, **137**, 303–317, doi:10.1002/qj.763.

Smith, R. B., 1980: Linear theory of stratified hydrostatic flow past an isolated mountain. *Tellus*, **32**, 348–364, doi:10.1111/j.2153-3490.1980.tb00962.x.

——, S. Skubis, J. D. Doyle, A. S. Broad, C. Kiemle, and H. Volkert, 2002: Mountain waves over Mont Blanc: Influence of a stagnant boundary layer. *J. Atmos. Sci.*, **59**, 2073–2092, doi:10.1175/1520-0469(2002)059<2073:MWOMBI>2.0.CO;2.

——, B. K. Woods, J. Jensen, W. A. Cooper, J. D. Doyle, Q. F. Jiang, and V. Grubisic, 2008: Mountain waves entering the stratosphere. *J. Atmos. Sci.*, **65**, 2543–2562, doi:10.1175/2007JAS2598.1.

Smith, S. A., D. C. Fritts, and T. E. VanZandt, 1987: Evidence for a saturated spectrum of atmospheric gravity waves. *J. Atmos. Sci.*, **44**, 1404–1410, doi:10.1175/1520-0469(1987)044<1404:EFASSO>2.0.CO;2.

——, J. Baumgardner, and M. Mendillo, 2009: Evidence of mesospheric gravity-waves generated by orographic forcing in the troposphere. *Geophys. Res. Lett.*, **36**, L08807, doi:10.1029/2008GL036936.

Sonmor, L. J., and G. P. Klaassen, 1997: Toward a unified theory of gravity wave stability. *J. Atmos. Sci.*, **54**, 2655–2680, doi:10.1175/1520-0469(1997)054<2655:TAUTOG>2.0.CO;2.

Sutherland, B. R., 2010: *Internal Gravity Waves.* Cambridge University Press, 377 pp.

Swenson, G. R., M. J. Taylor, P. J. Espy, C. Gardner, and X. Tac, 1995: ALOHA-93 measurements of intrinsic AGW characteristics using airborne airglow imager and ground-based Na wind/temperature lidar. *Geophys. Res. Lett.*, **22**, 2841–2844, doi:10.1029/95GL02579.

Taylor, M. J., and M. A. Hapgood, 1988: Identification of a thunderstorm as a source of short period gravity waves in the upper atmospheric airglow emissions. *Planet. Space Sci.*, **36**, 975–985, doi:10.1016/0032-0633(88)90035-9.

——, Y. Y. Gu, X. Tao, C. S. Gardner, and M. B. Bishop, 1995: An investigation of intrinsic gravity wave signatures using coordinated lidar and nightglow image measurements. *Geophys. Res. Lett.*, **22**, 2853–2856, doi:10.1029/95GL02949.

Thomas, L., R. M. Worthington, and A. J. McDonald, 1999: Inertia-gravity waves in the troposphere and lower stratosphere associated with a jet stream exit region. *Ann. Geophys.*, **17**, 115–121, doi:10.1007/s005850050741.

Tsuda, T., T. Inoue, D. C. Fritts, T. E. VanZandt, S. Kato, T. Sato, and S. Fukao, 1989: MST radar observations of a saturated gravity wave spectrum. *J. Atmos. Sci.*, **46**, 2440–2447, doi:10.1175/1520-0469(1989)046<2440:MROOAS>2.0.CO;2.

——, Y. Murayama, M. Yamamoto, S. Kato, and S. Fukao, 1990: Seasonal variation of momentum flux in the mesosphere observed with the MU radar. *Geophys. Res. Lett.*, **17**, 725–728, doi:10.1029/GL017i006p00725.

——, ——, H. Wiryosumarto, S. W. B. Harijono, and S. Kato, 1994: Radiosonde observations of equatorial atmospheric dynamics over Indonesia: 2. Characteristics of gravity waves. *J. Geophys. Res.*, **99**, 10 507–10 516, doi:10.1029/94JD00354.

Vincent, R. A., and I. M. Reid, 1983: HF Doppler measurements of mesospheric momentum fluxes. *J. Atmos. Sci.*, **40**, 1321–1333, doi:10.1175/1520-0469(1983)040<1321:HDMOMG>2.0.CO;2.

Vosper, S. B., 2015: Mountain waves and wakes generated by South Georgia: Implications for drag parameterization. *Quart. J. Roy. Meteor. Soc.*, **141**, 2813–2827, doi:10.1002/qj.2566.

Walterscheid, R. L., J. H. Hecht, R. A. Vincent, I. M. Reid, J. Woithe, and M. J. Hickey, 1999: Analysis and interpretation of airglow and radar observations of quasi-monochromatic gravity waves in the upper mesosphere and lower thermosphere over Adelaide, Australia (35°S, 138°E). *J. Atmos. Sol.-Terr. Phys.*, **61**, 461–478, doi:10.1016/S1364-6826(99)00002-4.

Wang, L., D. C. Fritts, B. P. Williams, R. A. Goldberg, F. J. Schmidlin, and U. Blum, 2006: Gravity waves in the middle during the MaCWAVE winter campaign. *Ann. Geophys.*, **24**, 1209–1226, doi:10.5194/angeo-24-1209-2006.

Warner, C. D., and M. E. McIntyre, 1996: On the propagation and dissipation of gravity wave spectra through a realistic middle atmosphere.

J. Atmos. Sci., **53**, 3213–3235, doi:10.1175/1520-0469(1996)053<3213:OTPADO>2.0.CO;2.

Whiteway, J. A., and A. I. Carswell, 1994: Rayleigh lidar observations of thermal structure and gravity wave activity in the high Arctic during a stratospheric warming. *J. Atmos. Sci.*, **51**, 3122–3136, doi:10.1175/1520-0469(1994)051<3122:RLOOTS>2.0.CO;2.

——, E. G. Pavelin, R. Busen, J. Hacker, and S. Vosper, 2003: Airborne measurements of gravity wave breaking at the tropopause. *Geophys. Res. Lett.*, **30**, 2070, doi:10.1029/2003GL018207.

Williams, B. P., D. C. Fritts, C. Y. She, G. Baumgarten, and R. A. Goldberg, 2006: Gravity wave propagation, tidal interaction, and instabilities in the mesosphere and lower thermosphere during the winter 2003: MaCWAVE rocket campaign. *Ann. Geophys.*, **24**, 1199–1208, doi:10.5194/angeo-24-1199-2006.

Woodman, R. F., and A. Guillen, 1974: Radar observations of winds and turbulence in the stratosphere and mesosphere. *J. Atmos. Sci.*, **31**, 493–505, doi:10.1175/1520-0469(1974)031<0493:ROOWAT>2.0.CO;2.

Wu, D. L., and S. D. Eckermann, 2008: Global gravity wave variances from Aura MLS: Characteristics and interpretation. *J. Atmos. Sci.*, **65**, 3695–3718, doi:10.1175/2008JAS2489.1.

Yamashita, C., H.-L. Liu, and X. Chu, 2010: Gravity wave variations during the 2009 stratospheric sudden warming as revealed by ECMWF-T799 and observations. *Geophys. Res. Lett.*, **37**, L22806, doi:10.1029/2010GL045437.

Yeh, K. C., and C. H. Liu, 1981: The instability of atmospheric gravity waves through wave-wave interactions. *J. Geophys. Res.*, **86**, 9722–9728, doi:10.1029/JC086iC10p09722.

AMS BOOKS: HISTORY • CLIMATE • WEATHER

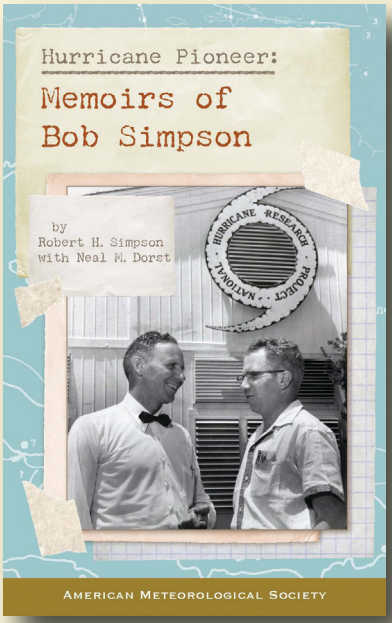

HURRICANE PIONEER

Memoirs of Bob Simpson

Robert H. Simpson with Neal M. Dorst

In 1951, Bob Simpson rode a plane directly into the wall of a hurricane—just one of his many pioneering explorations. This autobiography of the first director of the National Hurricane Research Project and co-creator of the Saffir-Simpson Hurricane Scale starts with childhood remem-mbrance and ends in first-hand account of a revolutionary

© 2014, PAPERBACK
ISBN: 978-1-935704-75-1
LIST $30 MEMBER $20

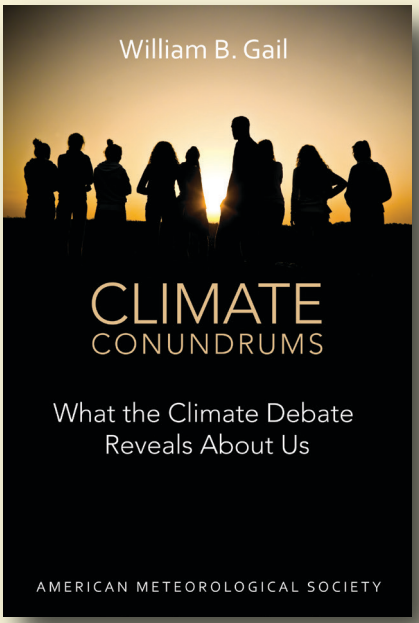

CLIMATE CONUNDRUMS

What the Climate Debate Reveals About Us

William B. Gail

This is a journey through how we think, individually and collectively, derived from the climate change debate. With wit and wisdom, Gail explores several questions: Can we make nature better? Could science and religion reconcile? Insights from such issues can help us better understand who we are and help

© 2014, PAPERBACK
ISBN: 978-1-935704-74-4
LIST $30 MEMBER $20

Browse online at
ametsoc.org/bookstore

FREE SHIPPING
for AMS Members!

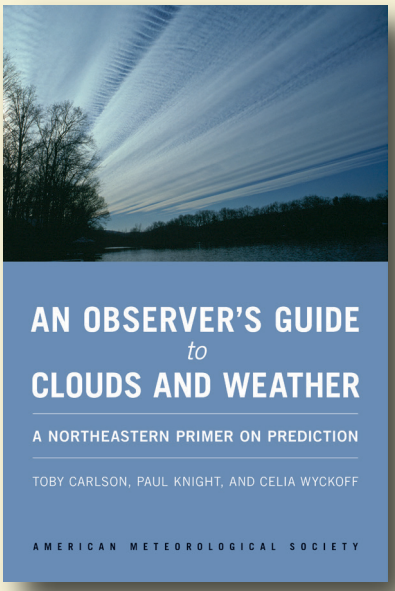

AN OBSERVER'S GUIDE TO CLOUDS AND WEATHER

A Northeast Primer on Prediction

Toby Carlson, Paul Knight, and Celia Wyckoff

With help from Penn State experts, start at the beginning and go deep. This primer for enthusiasts and new students alike will leave you with both refined observation skills and an understanding of the complex science behind the weather: the ingredients for making reliable predictions of your own.

© 2014, PAPERBACK
ISBN: 978-1-935704-58-4
LIST $35 MEMBER $20

AMS BOOKS

AMS Books are available to groups and booksellers, and desk copies may be obtained, through our distributor The University of Chicago Press: 1-800-621-2736 or custserv@press.uchicago.edu.